UNIVERSITY OF CALIFORNIA SAN DIEGO

Design and Evaluation of a Miniaturized Wireless Force Sensor Based on Wave Backscattering

A thesis submitted in partial satisfaction of the
requirements for the degree of Master of Science

in

Engineering Sciences (Mechanical Engineering)

by

Daegue Park

Committee in charge:

Professor Tania Morimoto, Chair
Professor Dinesh Bharadia
Professor James Friend
Professor Lisa Poulikakos

2022

The Thesis of Daegue Park is approved, and it is acceptable in quality and form for publication on microfilm and electronically.

University of California San Diego

2022

DEDICATION

I would like to dedicate my thesis to my beloved parents.

TABLE OF CONTENTS

LIST OF FIGURES

LIST OF TABLES

ACKNOWLEDGEMENTS

First and foremost, I would like to express my deep and sincere gratitude to my advisor Professor Tania Morimoto who made this work possible. Her invaluable support, encouragement, and guidance carried me throughout the research process. Also, she has taught me the methodology to carry out the research and present the research works as clearly as possible. It was a great privilege for me to work and study under her guidance.

Next, I would like to thank the other members of my committee. In particular, I would like to thank Professor Dinesh Bharadia for providing suggestions and comments on the sensor's wireless communication, which undoubtedly shined this work. Additionally, I would like to thank Professor James Friend and Professor Lisa Poulikakos for their insightful comments and questions, which made me think deeper about the project and led to new ideas for future work.

Further, I would like to thank the members I collaborated with: Dr. Cédric Girerd provided valuable help and advice throughout the process, and Agrim Gupta and Shayaun Bashar paved the way for wireless communication and the sensor interface. The stimulating discussions with them helped me broaden my perspective in research and grow to be a more professional academic researcher.

Last but not least, I would like to thank all the members of Morimoto Lab for their encouragement, support, advice, and all the fun we had, which kept me going during this entire project.

This thesis, in part, has been submitted for publication of the material as it may appear in IEEE Robotics and Automation Letters, 2022, Park, Daegue; Gupta, Agrim; Bashar, Shayaun; Girerd, Cédric; Bharadia, Dinesh; Morimoto, Tania K., and Proceedings of the ACM on Interactive, Mobile Wearable and Ubiquitous Technologies, 2022, Gupta Agrim; Park, Daegue; Bashar, Shayaun; Girerd, Cédric; Morimoto, Tania K.; Bharadia, Dinesh. The thesis author was the primary author and co-author of these papers, respectively.

ABSTRACT OF THE THESIS

Design and Evaluation of a Miniaturized Wireless Force Sensor Based on Wave Backscattering

by

Daegue Park

Master of Science in Engineering Sciences (Mechanical Engineering)

University of California San Diego, 2022

Professor Tania Morimoto, Chair

The ability to sense forces is critical for ensuring that robots can safely interact with their environment. Nevertheless, there are numerous situations, particularly for medical applications, where environmental and sensor density requirements can pose challenges and constraints to sensor design and implementation. Our previous work presented a novel wireless force sensing paradigm and developed a force sensor based on wave backscattering. However, its large size, rigid design, and the need for an external power supply limited its practical use in medical applications. This work presents a significantly improved and miniaturized force sensor design with wireless and battery-free functions based on a new novel working principle. An end-to-end simulation of the proposed sensor, its fabrication, modeling, and experimental validations in

a wired setting is presented. Then, flexible, wireless, and battery-free functions are added to the sensor by improving the sensor interfaces. The sensor performance in a wireless setting is evaluated, and the wireless communication quality is tested to validate the sensor's suitability for medical applications. The proposed sensor can sense forces from 0 N to 6 N. In a wired setting, the sensor's average Root Mean Square (RMS) error was 0.15 N and showed a resolution as high as 0.42 mN. In a wireless setting, the RMS error of the sensor was 0.21 N and had a resolution as high as 150 mN for our sensor prototypes with different interfaces. A demonstration of contact force sensing with the proposed sensors mounted on the body of a continuum robot and a phantom test is presented to show its potential to enable applications in fields such as medical robotics.

Chapter 1

Introduction

Sensors are a critical component of robotic systems, necessary for ensuring safety and precision during the execution of complex tasks. As robots transition into operating in more constrained and sensitive environments, including inside the human body, force sensors in particular, become increasingly important. Force information can help prevent damage to the surrounding environment [1], improve robot control during delicate tasks [2], and even estimate the deflection of the robot itself in the case of soft and flexible robots [3]. However, there are many scenarios where integrating existing force sensors becomes challenging to impossible based on incompatibility with the environment of use or because of their size, stiffness, or general form factor [4]. We focus here on developing a new force sensor to overcome these challenges for applications in medical robotics, starting with applications in, for example, cardiothoracic [5, 6, 7], laparoscopic [8, 9, 10], and urologic [11, 12, 13] procedures.

1.1 Force Sensors for Medical Robots

Force sensing is crucial for medical applications [14, 15]. For example, for teleoperated surgical robots, real-time force measurements can provide surgeons with direct feedback on the applied forces rather than leaving them to rely on visual feedback alone [16]. Therefore, this force information can help minimize damage to surrounding tissues by ensuring that applied forces are limited to safe levels [17]. Several force sensing technologies have been proposed for

medical applications (see [16] for a detailed review). Such sensors include, for example, strain gauges [18], piezoelectric [19], optical [20], magnetic [21], and capacitive [22] sensors. While these sensing technologies can provide high accuracy measurements with small form factors, they are usually wired, which poses integration issues for sensing forces along with a 1-D or 2-D space.

Indeed, it can be essential to measure forces applied along the entire length of a robot, particularly in the case of flexible, continuum robots [23]. The shape of these robots can be affected by loads induced during interaction with the environment, and the integration of sensors can help improve shape estimation and control. While many types of sensors have been developed to measure or estimate the shape of continuum robots, including optical fibers, FBG and light intensity sensors, and electromagnetic and optical trackers [24], they usually provide an indirect and incomplete way of estimating forces. Further, solving for force magnitude and location from the observed deformed shape of robots has proved to have some crucial limitations [25]. In particular, such methods have typically been sensitive to the robot stiffness and the tracking system's accuracy [25], and cannot be used to estimate antagonistic applied forces. Researchers have also proposed force sensors for flexible instruments and continuum robots and have integrated them on their bodies [19, 26] in order to measure such information directly.

1.2 Miniaturized Wireless Force Sensors

Despite advancements in the development of force sensors for medical robots, there still remain challenges with measuring forces across the entire robot surface, particularly when space must be reserved for the passage of surgical instruments. Researchers have proposed a few main approaches for wireless force sensors that can help overcome these challenges. These approaches include LC resonant sensors [27], NFC based sensors [19], and SAW-based strain sensors [28]. However, these sensors have very low interrogation distances and have not been

shown to work reliably in a realistic environment where wireless signals undergo rich scattering effects [29].

While we proposed a sensor paradigm for wireless usage based on Radio Frequency (RF) backscattering [30, 31] to address these challenges for wireless force sensors, the associated mechanical architecture was not well-suited for miniaturization. It relied on a change in contact location between a signal and ground trace, in order to change the total travel distance of a reflected electromagnetic wave as $\Delta S_{phase} = \gamma \Delta x$, where $\gamma = \frac{2\pi f}{c}$, Δx is the difference in travel distance of the wave, and f is the frequency of the wave. Because the maximum travel distance of the wave is directly related to the sensor length, decreasing the sensor length for miniaturization would result in a smaller range of S_{phase} and, therefore, lower sensing resolution [30].

While increasing the frequency could allow for smaller designs, there is an upper bound at 1 GHz [32, 33, 34] since higher frequencies cannot easily penetrate human tissue. The overall result of relying on changes in contact trace locations to induce phase change is that micro or millimeter-scale sensors would lead to only minimal phase shifts. To overcome this limitation, we propose a new, capacitor-like design, which relies on impedance change as a signal trace gets closer to a ground trace rather than on a length change-induced phase change.

1.3 Contributions

The contributions of this work are as follows. First, we present a new type of capacitive-based sensor design that relies on the wave backscattering principle. It is different in its working mechanism compared to our previous work, as it is no longer based on a change in contact location between a signal and ground trace, which poses miniaturization issues. Instead, it is based on a change of induced impedance as the distance between such traces varies. Second, we propose a multiphysics model of the sensor that can be used to simulate its behavior, as design parameters are varied. Third, we use the developed multiphysics model to design and fabricate sensor prototypes. The sensors are designed to measure forces between 0 N to 6 N to

accommodate various surgical procedures. We demonstrate the sensor's potential for measuring forces applied to the body of a continuum robot. Finally, we make the sensor flexible, wireless, and battery-free by interfacing it with RFID tags and a flexible antenna and PCB. We evaluate the sensor's performance in a wireless testing environment, as well as in phantoms, and test the wireless communication quality.

Chapter 2

Sensor Modeling

This chapter describes the sensor's new working principle and presents an end-to-end simulation for design purposes.

2.1 Working principle

The working principle relies on a change in capacitance, and therefore impedance, to convert an applied force into a phase of a backscattered wave. The capacitive-based sensor is composed of three layers: a conductive layer on the top and the bottom and a soft polymer layer in between. The bottom conductive layer is connected to a signal trace, while the top one is grounded. The soft polymer layer effectively acts like a dielectric medium separating the conductive layers, similar to a parallel plate capacitor, as illustrated in Fig. 2.1.

The initial capacitance of the sensor at steady-state is $C = \varepsilon \frac{A}{d}$, where ε is the dielectric permittivity, A is the surface area of the conductive plates, and d is the distance between them. As a force is applied to the sensor, the soft polymer deforms and brings the conductive layers closer together, leading to an increase in the sensor capacitance. Hence, the sensor capacitance is a function of applied force, denoted as $C(F)$, where F is the force applied. From an Radio Frequency (RF) perspective, this change in capacitance leads to a change in the sensor impedance, given by $Z = \frac{1}{j\omega C(F)}$, where $\omega = 2\pi f$ and f is the frequency of the input wave. This change in impedance results in a change in the phase of the wave, since

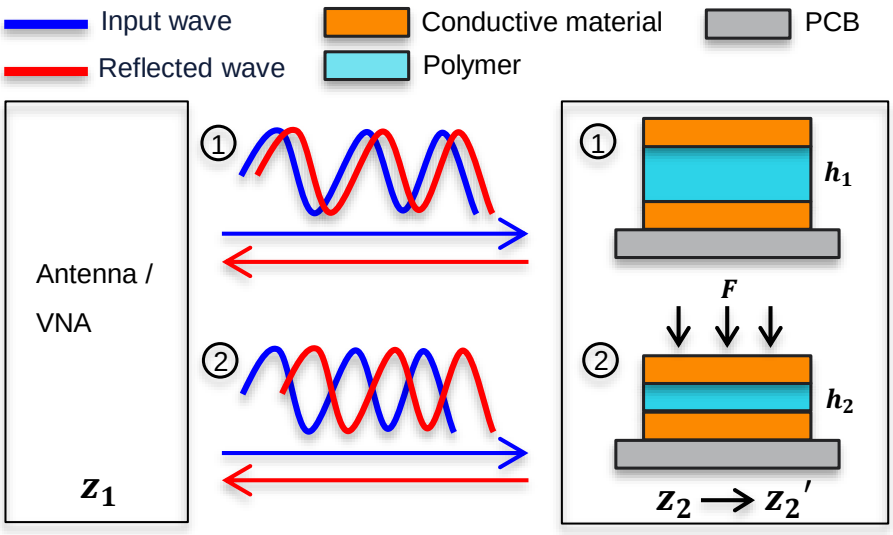

Figure 2.1. Illustration of the working principle of the proposed sensor. As a force is applied, the soft polymer layer deforms and brings the conductive layers closer together, leading to a change in the sensor's impedance, which changes the phase of a reflected RF signal.

$S_{phase} = 2\tan^{-1}(\frac{1}{Z_{in}\omega C(F)})$, where Z_{in} is the input impedance. Therefore, the external force causes a phase difference between the transmitted and reflected wave, as illustrated in Fig. 2.1. Further, capacitive-based model of the sensor enables its response to frequencies which leads to its wireless communication capability.

2.2 End-to-End Simulation

We created an end-to-end Finite Element Analysis (FEA) simulation that models both the mechanical and RF components of our sensor and that can be used to determine a set of sensor design parameters for a given application. To do so, we used COMSOL Multiphysics to simultaneously capture the sensor's mechanical behavior — using the Solid Mechanics module — and the phase shift between a transmitted and reflected wave — using the RF module. Details on both components, as well as details on our design parameter selection, are given below.

Mechanical Component: Ecoflex 00-30 was selected for the dielectric polymer layer due to its high stretchability, durability, and ability to deform under applied loads while not

yielding or fracturing under the maximum mechanical stress and strain level experienced. In order to simulate the non-linear hyperelastic mechanical behavior of Ecoflex 00-30, the Yeoh model was used with $C_1 = 17$ kPa, $C_2 = -0.2$ kPa, $C_3 = 0.023$ kPa [35]. The Ecoflex 00-30 was considered to be nearly incompressible and the initial bulk modulus used in our simulations was calculated using the relationship $K = \frac{E}{3(1-2\nu)}$, with a Young's modulus $E = 125$ kPa [36] and a Poisson's ratio $\nu = 0.49$. Rather than connecting the conductive layers of the sensor with wires carrying the 900 MHz signals, which would result in signal leakages, the PCB was used to robustly excite the sensor. Additionally, the PCB provides a support and connection interface for our sensor prototypes. Therefore, for validation purposes, we mounted the sensor onto a PCB microstrip line that was integrated into our simulation.

RF Component: In order to simulate the wave backscattering capabilities of the sensor, we must excite it at a given RF frequency and observe the phase of the reflected signal. We choose a frequency of 900 MHz among the possible sub-1 GHz frequency bands, because it has been widely used for in-vivo wireless backscatter sensing and has been shown to work robustly even when the signals go though multiple tissue layers [31, 33, 34]. The PCB was selected to have a standard 50 Ω impedance and implements a 900 MHz matched microstrip line, which acts as a stable, loss-less medium of propagation for the electromagnetic waves. The top copper layer of the sensor is connected to the ground trace of the PCB with a 20 µm diameter tungsten wire, and the bottom copper layer of the sensor is placed directly onto the signal trace of the PCB, as illustrated in Fig. 2.2.

Since the diameter of the tungsten wire is 100 times smaller than the polymer layer thickness, its impact on the sensor geometry and stress level was negligible in the simulation. Also, it is observed that its location on the polymer layer does not significantly affect the phase output of the sensor. The port was assigned at the end of the microstrip line on the PCB. The characteristic impedance of the input wave is set to the same impedance as the PCB, 50 Ω, to maximize wave transmission between the port and the PCB. Additionally, the port phase

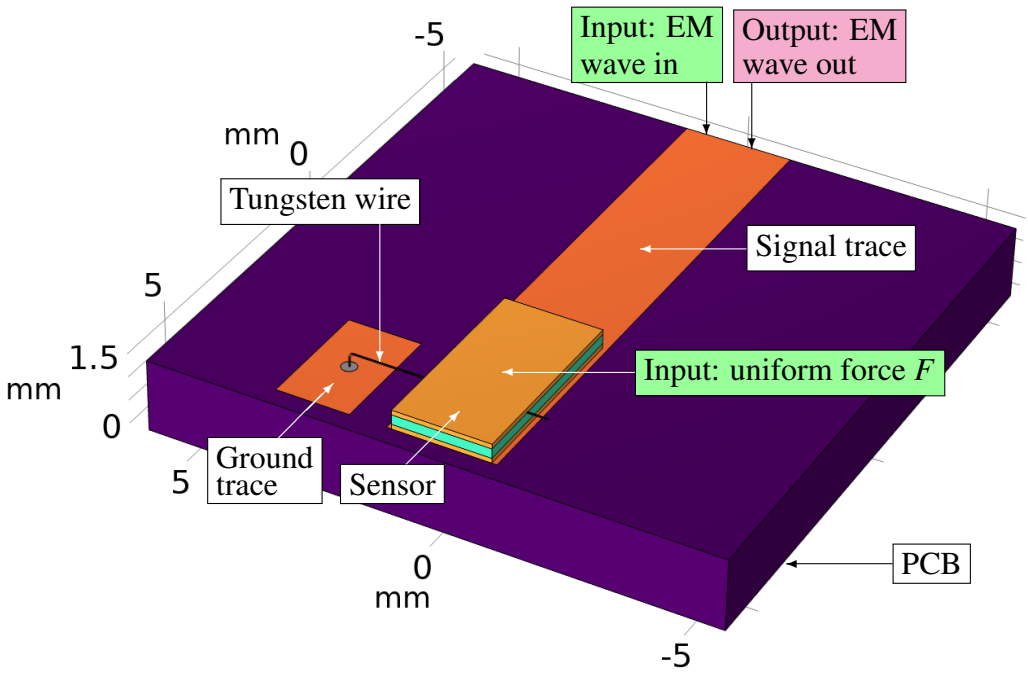

Figure 2.2. Model of the sensor, PCB, signal trace, ground trace, and tungsten wire, as implemented in COMSOL Multiphysics.

was set to 0 ° for the ease of observing phase shift. Electromagnetic waves propagate along the microstrip line on the PCB, which is a signal trace, visible in Fig. 2.2. Once they reach the sensor, they are reflected and travel back to the original port. With a single port used in the simulation, these signal reflections are typically characterized by the reflection scattering parameter, S_{11}, which describes the ratio of magnitudes S_{mag} and phase differences S_{phase} of input and output signals. First, the magnitude, $S_{mag} = |S_{11}|$, of the signal must lie between 0 dB and -1 dB to ensure that the majority of the input wave is backscattered without signal loss. The significance of S_{mag} in a wired communication seems trivial, however, since the ultimate goal is to read the sensor output in a wireless setting where the signal power is an important factor for the reliable wireless communication, it was important to both simulate and test S_{mag} in simulation and fabrication steps. Next, the phase, $S_{phase} = \angle(S_{11})$, is used as our main metric to evaluate the sensor performance across the various sensor designs assessed. Indeed, a large phase shift over the range of applied forces leads to a higher sensitivity and resolution of the

applied force magnitude estimation.

Parameter Selection: The final step once both the mechanical and RF components of the sensor are fully set up, is to solve for a set of design parameters that will result in sufficient phase shift over the force range required for the particular application. We start here by designing a sensor applicable across a wide range of surgical procedures. Given that the mean of the average of measured forces has been reported to range from 0.04 N to 5.70 N for different surgical specialties — including ophthalmology, vascular surgery, neurosurgery, cardiothoracic surgery, general surgery, and urologic surgery [11, 17] — we selected to design our proposed sensor for use within this general range of 0 N to 6 N. To understand the effects of varying each design parameter on the sensor performance, a range and step size was first selected for each parameter as follows: the thickness of copper and Ecoflex 00-30 layers were increased from 0.1 mm to 0.5 mm with a step size of 0.1 mm, and the width and length of the sensor were increased from 1 mm to 5 mm with a step size of 1 mm. Designs were then simulated under applied loads in the range of 0 N to 6 N with a step size of 1 N, resulting in the following general trends between the design parameters and scattering parameters. Overall, decreasing each design parameter resulted in minimal changes to the S_{mag} value, and all designs resulted in ranges of S_{mag} between 0 dB and -1 dB. In addition, decreasing each design parameter led to an increase in the range of S_{phase}. While maximizing this range of S_{phase} over the range of applied forces is desirable to enable higher sensitivity and resolution, the manual fabrication techniques used, set a lower limit on the feasible design parameters. For some sets of parameters, the sensor fabrication was challenging. Since all fabrication processes were done manually, fabrication and usage of 0.1 mm thick Ecoflex 00-30 and 1 mm wide copper, for example, was challenging and made it hard to fabricate sensors with repeatable results. Therefore, considering both the scattering parameters for wireless capabilities and sensor resolution, and the limits of our process for ease of fabrication and reproducilbility, the following set of values was chosen for the final sensor dimensions: 0.1 mm for the copper thickness, 0.2 mm for the Ecoflex 00-30

thickness, 2.0 mm for the sensor width, and 4.0 mm for the sensor length as shown in Fig. 2.3.

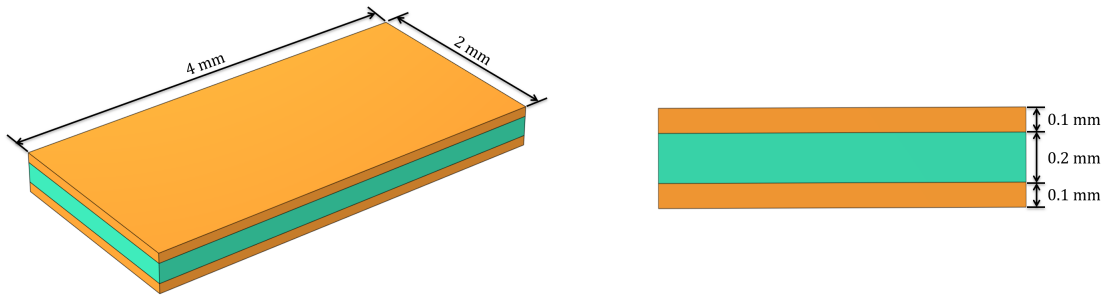

(a) **(b)**

Figure 2.3. Final dimensions of the sensor, with (a) width and length of the sensor, and (b) thickness of each layer.

Simulation Results: Overall, this design showed a linear change in phase of 15.05 ° over 0 N to 6 N of force in COMSOL simulation, as visible in Fig. 2.4.

This full scale output (i.e. maximum phase change over the designed range of forces) would give the sensor a sensitivity of 2.51 °/N. Since the resolution of the sensor depends on the resolution of the testing equipment, the sensor resolution was calculated for both wired and wireless testing environment. In a wired setting with a 0.01 ° resolution VNA (Vector Network Analyzer, E5071C Agilent Technologies), the sensor resolution would be 4 mN. Considering the wireless compatibility of the sensor, the sensor resolution would be 0.4 N in a wireless setting

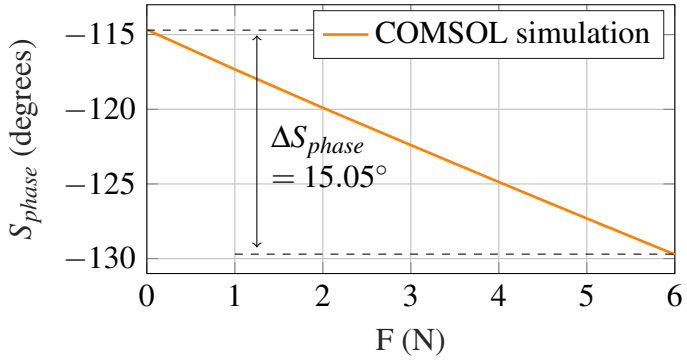

Figure 2.4. COMSOL simulation results for our sensor with the selected design parameters. As the force applied to the sensor increases, the phase of the reflected wave decreases.

with 1 ° resolution as evaluated in our previous work [31]. Given that the sensor resolution should be at least one order of magnitude less than the force difference to be resolved (in order to reduce the effect of quantization error) [37], wired sensor resolutions would be sufficient for surgical applications that require force measurements of 0.04 N to 6 N.

Chapter 3

Sensor Fabrication

The sensors are then fabricated based on the final simulated design. The first step is to fabricate each component of the sensor, including the copper layers and the polymer layer. A DCH-355-3 Laser (Photonics Industries International, Inc.) was used to laser cut the 0.1 mm thick copper sheets into the desired dimensions (2 mm $\times$ 4 mm). To prepare the polymer layer, Ecoflex 00-30 part B was pre-mixed thoroughly for 30 seconds and then combined with a weight ratio of 1:1 with part A. After mixing for 3 minutes, the mixture was vacuum degassed at -1 Bar for 5 minutes. The mixture was then blade coated with a height of 0.2 mm on a glass slide. This polymer layer sat at room temperature for 4 hours and was then post-cured at 80 °C for an additional 2 hours to allow it to reach its maximum performance properties [38].

Once the components are prepared, the next step is to combine the layers to form the full sensor. In order to remove a variety of contaminants from surfaces and to increase adhesion between the conductive and polymer layers, every interface was UV/Ozone (UVO) treated for 60 seconds (UVO-Cleaner Model 42, Jelight Company, Inc.). As seen in Fig. 3.1, one side of a pre-cut copper piece and one side of the cured Ecoflex 00-30 were UVO treated.

Ecoflex-0030 was then cut to meet the desired size specifications and placed onto the UVO-treated bottom copper layer with the UVO-treated surfaces facing each other. Next, the other side of the Ecoflex 00-30 layer and the top copper layer were then UVO treated. Finally, a 8 mm long tungsten wire with diameter of 20 µm was placed across the top of the Ecoflex 00-30,

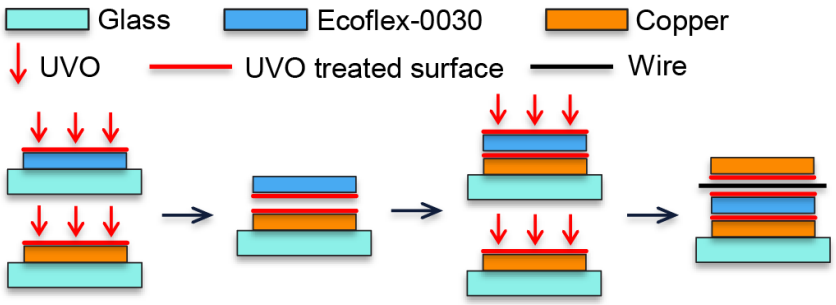

Figure 3.1. Illustration of the fabrication steps for the sensor.

and the top layer copper was placed on top of the wire with the UVO-treated surface facing down. The fabricated sensor, shown from both the top (Fig. 3.2a) and side (Fig. 3.2b), was left to sit for 2 hours at room temperature to ensure a strong adhesion between the layers.

The fabricated sensor was then mounted onto the PCB (11.56 mm $\times$ 11.65 mm $\times$ 1.5 mm) with the tungsten wire side facing up. Since the maximum use temperature of Ecoflex 00-30 is 232 °C [38], solder paste with a melting point of 219 °C [39] was used to prevent deformation of the polymer at a high temperature. The bottom copper layer was soldered onto the signal trace of the PCB and the tungsten wire to the ground trace. The sensor attached to the PCB is shown in Fig. 3.2c.

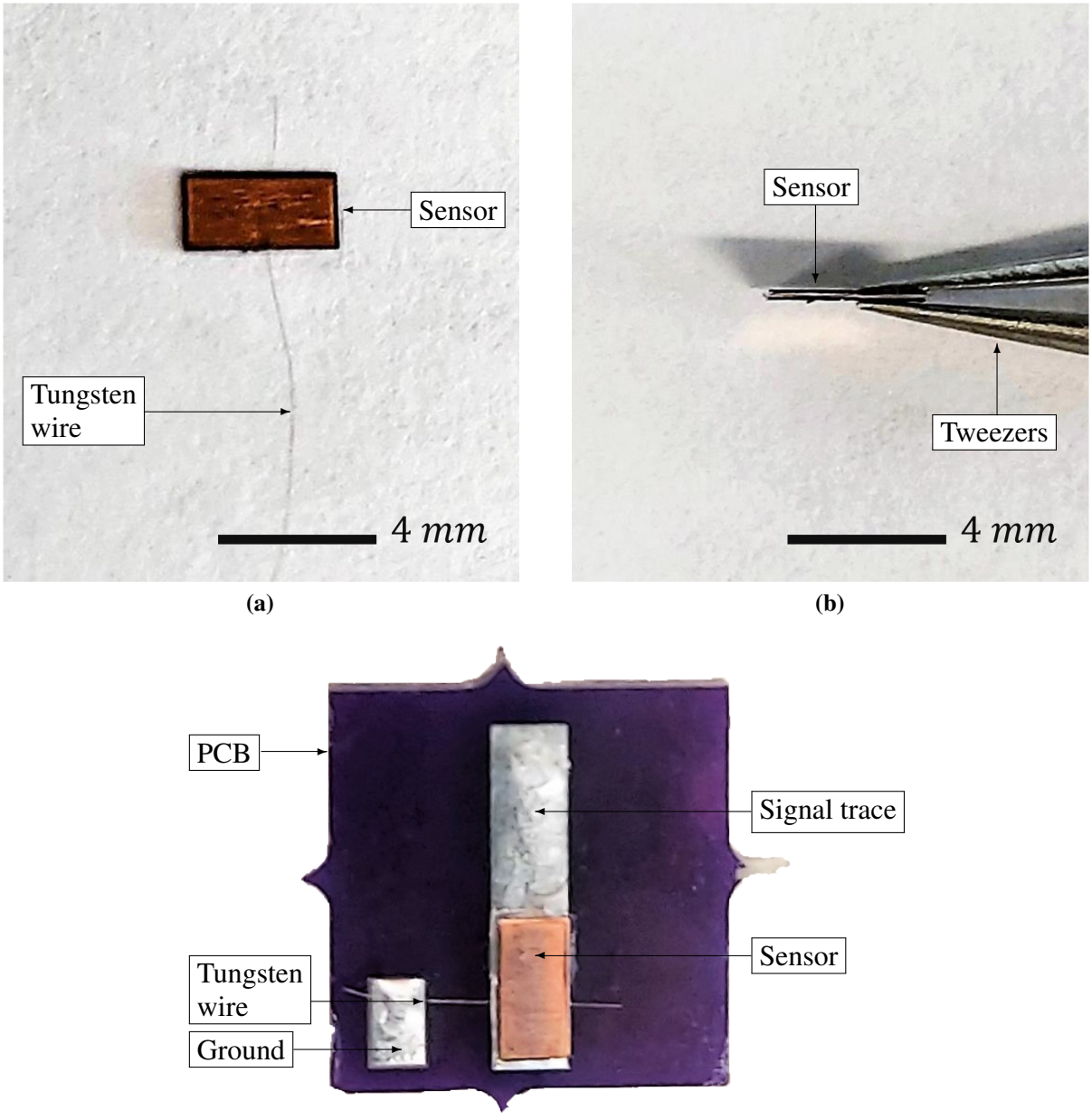

Figure 3.2. Photos of the final fabricated sensors, with (a) top view and (b) side view of one of the fabricated prototypes, and (c) top view of the same prototype after assembly on the PCB.

Chapter 4

Sensor Evaluation

To evaluate the sensor performance and verify it matches the simulation results, we perform the following experiments.

4.1 Experimental Setup

The experimental setup shown in Fig. 4.1 was designed to enable known forces to be applied to the fabricated sensors and subsequently compared to the output from the sensors themselves. Since only normal forces are being considered, it was critical to ensure that the indenter and sensor remained parallel throughout the experiments.

For this purpose, a linear actuator with a flat indenter is used to apply forces onto the sensor, which is mounted onto a load cell. The load cell, which provides the ground-truth measurements of the forces being applied, has a maximum measurable force of 49.5 N and an accuracy of 0.0098 N. The sensor itself is connected to a VNA with a U.FL cable [40] that enables phase measurements in a wired configuration. We note that the Intermediate Frequency bandwidth of the VNA is set to 70 kHz, which is sufficient for measuring forces with a temporal resolution of 35 kHz.

It should also be noted that environmental factors should be considered since they could affect the mechanical behavior of the polymer [41, 42] and frequency response of the sensor [43]. Evaluations were performed under an average ambient room temperature of 22 °C

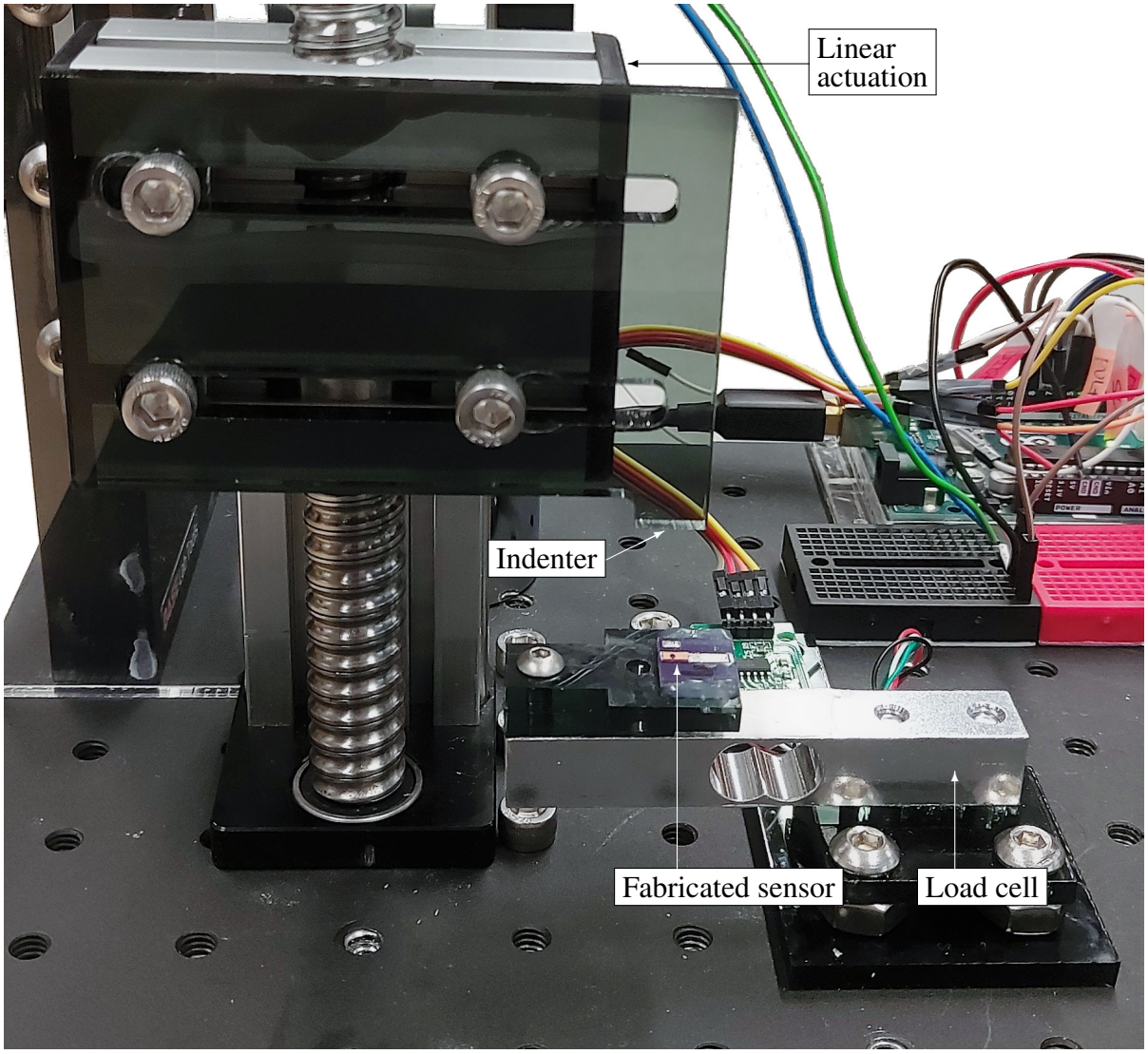

Figure 4.1. Experimental setup used for the evaluation of the sensors.

and relative humidity of 50 %. Only the soft polymer used in our sensor (Ecoflex 00-30) could be subject to changes in its mechanical behavior during a temperature change from 22 °C to 36.5 °C. However, since it is shown that Ecoflex 00-30 has similar mechanical behavior for temperatures between 20 °C and 60 °C [44], the sensor is expected to show similar performance even when used inside the human body (typically 36.5 °C). And since the sensor will ultimately be hermetically sealed, such that external moisture will be prevented from coming in contact with the sensor, the effects of changes in humidity were not seen as a major concern. Further, since

the electromagnetic fields generated by the human body typically have very low frequencies (few kHz [45]) compared to the 900 MHz working frequency of the sensor, it could be easily filtered out with the measuring equipment. Even with the electromagnetic noise from the neighboring environment, it would typically be in lower frequencies, below 30 MHz [46] as compared to the sensor's operating frequency of 900 MHz, and hence should not create much crosstalk.

Finally, for filled silicone rubbers, including Ecoflex 00-30, it is found that stress softening (also known as the Mullins effect) occurs during cycles of loading and unloading paths [47]. It has been shown that in order to mitigate the effects of stress softening and obtain consistent mechanical properties, silicone rubbers should be applied multiple cycles or pre-stretched at a higher strain or relaxed at a specific strain [44, 48]. These pre-treatments not only overcome stress softening, but also removes stress recovery and hysteresis. Since the stress softening increases progressively as the maximum stretch level rises [49], it was essential to pre-stretch the sensors for a number of cycles with the maximum force to obtain uniformity of the mechanical behavior. It was empirically found that the force-to-phase output of the sensor converges after 20 cycles. Therefore, every sensor was pre-conditioned with 20 initial cycles, with loads ranging from 0 N to 6 N and an average strain rate of 0.0019 s^{-1}, prior to data collection.

4.2 Experimental Results

As described in Section 4.1, the Mullins effect could be mitigated after pre-stretching and this phenomena was observed throughout the experimental results in Fig. 4.2a, 4.2b, and 4.2c.

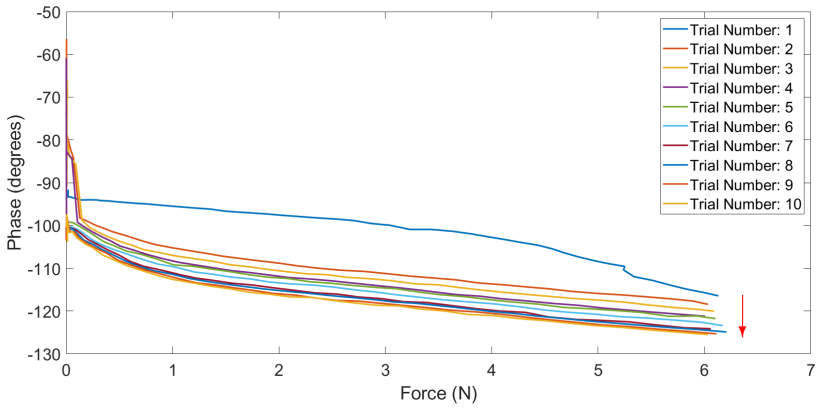

(a)

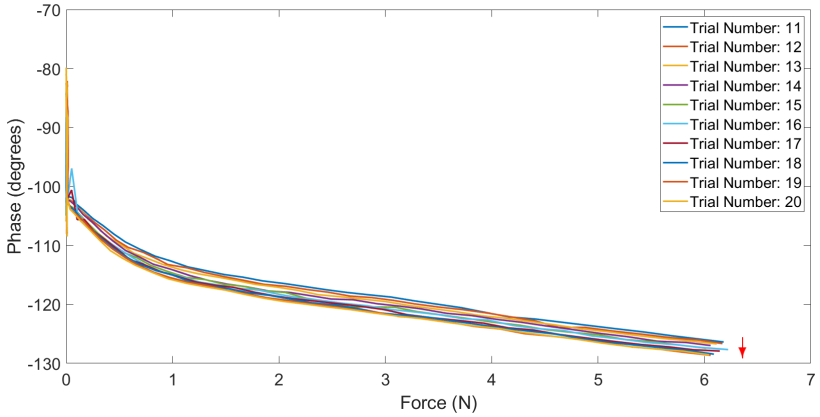

(b)

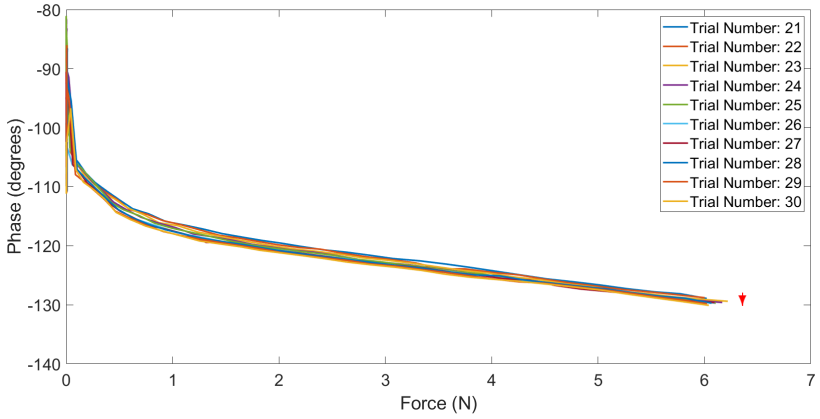

(c)

Figure 4.2. Results of the sensor showing Mullins effect, with (a) first 10 trials, (b) second 10 trials, and (c) third 10 trials. The force to phase graph converges after pre-treatment of initial 20 trials

Therefore, data for 10 loading cycles (trials 21-30) was collected after a pre-treatment of 20 trials for the two fabricated sensors to mitigate the Mullins effect. All trials are shown in purple in Fig. 4.3a and 4.3b. We note that as the trial number increases, there is a slight decrease in phase, which can likely be attributed to the Mullins effect.

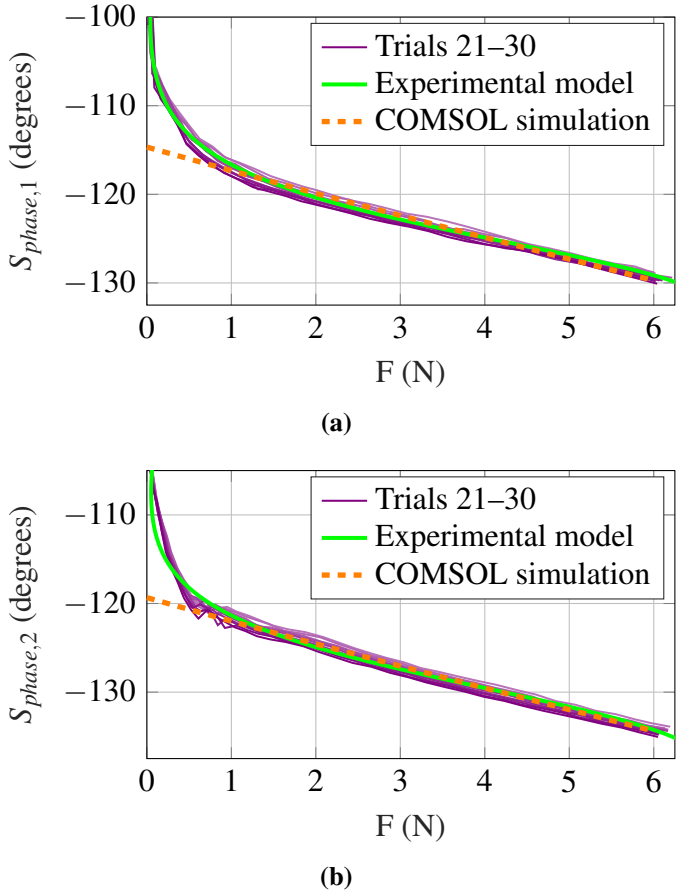

Figure 4.3. Plots of the experimental results for trials 21 to 30, the model created from the experimental data, and the results of the FEA for (a) sensor 1 and (b) sensor 2.

In addition, it is possible that the increase in the compressibility of Ecoflex 00-30 with an increased stretch ratio during the experiment could have created this difference between trials for both sensors [35]. However, the deviations are minimal, and it can be seen that across the range of applied loads, the measured phase remains relatively consistent from trial to trial. In addition, we note that even though there is an offset in phase between sensor 1 and sensor 2, the general shape and trend of the curves remain similar. The reason for this relative difference in

the initial phase can be attributed to the accuracy of fabrication and integration of the sensor to the PCB since these factors could affect the initial capacitance of the sensor and the phase of the input wave upon reaching the sensor, which is related to the distance between the sensor and the input port.

The experimental data was then compared to the FEA results presented in Section 2.2. Similarly, since electromagnetic waves backscatter upon reaching the sensor on the PCB, the sensor position on the PCB signal trace affects the initial phase of the reflected wave at a steady state. Therefore, any slight error in sensor placement on the signal trace creates an offset in starting phase compared to the simulation results. For comparison purposes, the obtained phases from our physical prototypes were shifted by adding an offset. The FEA results are visible in orange in Fig. 4.3a and 4.3b. It can be seen that in the force range of 0 N to 0.5 N the FEA results differ from the experimental data. This difference can likely be explained by the presence of tiny gaps or imperfect contact between the signal trace of the PCB and the bottom copper layer of the sensor, which were connected via a manual soldering process. If gaps exist, then the surface area of the sensor in contact changes as a force is applied until both surfaces are in full contact. This leads to a more significant change in sensor capacitance since the surface area and distance between conductive plates also become a function of the applied force, leading to an additional phase shift until the entire surface area contact happens. However, in the range of 0.5 N to 6 N, it can be seen that the phase obtained using FEA is overlapping well with the experimental data, with matching slopes. The comparison between the FEA results and the experimental data is satisfying and indicates that the FEA was successful in providing guidance for the sensor design in order to obtain the desired phase shift.

A model was then computed for each sensor to estimate the force for a measured phase and evaluate the sensor performance. A 2^{nd} order rational was used to curve fit the experimental data and is given by,

$$F(S_{phase,i}) = \frac{p_1 S_{phase,i}^2 + p_2 S_{phase,i} + p_3}{S_{phase,i}^2 + q_1 S_{phase,i} + q_2}, \tag{4.1}$$

where the coefficients used for each sensor model are given in Table 4.1.

Table 4.1. Corresponding coefficients of the experimental model for sensors 1 and 2.

Coefficients	p_1	p_2	p_3	q_1	q_2
$S_{phase,1}$	1.058	214.5	10910	257.2	16680
$S_{phase,2}$	1.465	317.4	17230	264.6	17670

The sensor models are also shown in green in Fig. 4.3a and 4.3b and show a qualitatively good fit. The RMS errors between the experimental model and the experimental data is 0.16 N and 0.18 N for sensors 1 and 2, respectively. In addition, the full scale output of each sensor can be evaluated, and is found to be 27.77 ° and 25.93 ° for sensor 1 and sensor 2, respectively. Using the constructed sensor models and the full scale output, the sensitivity and resolution of each sensor can then be evaluated for the two main regions visible in Fig. 4.3a and Fig. 4.3b — forces below 0.5 N and forces above 0.5 N. As shown in Table 4.2, the sensitivity and resolution for sensor 1 were 23.83 °/N and 0.42 mN for 0-0.5 N, and 2.88 °/N and 3.47 mN for 0.5-6 N. The sensitivity and resolution for sensor 2 were 19.82 °/N and 0.5 mN for 0-0.5 N, and 2.91 °/N and 3.43 mN for 0.5-6 N. Overall, these resolutions in both regions for two sensors are sufficient for many surgical applications [37] as the required resolution for targeted medical application is discussed in Section 2.2.

Table 4.2. Sensitivity and resolution of sensor 1 and sensor 2

Force range	0 - 0.5 N		0.5 - 6 N	
Metric	Sensitivity	Resolution	Sensitivity	Resolution
Sensor 1	23.83 °/N	0.42 mN	2.88 °/N	3.47 mN
Sensor 2	19.82 °/N	0.5 mN	2.91 °/N	3.43 mN

It can be seen that the two sensors showed some slight differences in terms of RMS errors, full scale output, sensitivity, and resolution. These differences could be due to errors in the manual fabrication process, including errors in the dimensions of each layer or in the geometry of the sensor during their assembly. In addition, due to possible imperfect parallelism between the indenter and the top surface of the sensor during evaluation, the applied force may not have been perfectly uniform or may have included shear components which could have caused the error in sensor performance. These possible errors could be minimized with a more precise fabrication process and experimental setup in the future.

In summary, the developed sensors, sensor 1 and sensor 2, were able to resolve force differences as small as 34.7 mN and 34.3 mN, respectively, for the entire force range of 0 N to 6 N which meets our design requirements.

Chapter 5

Sensor Demonstration

In this chapter, we propose a realistic use case for our sensors, by attaching them to a tendon-driven robot. We then compare the estimated forces applied to the sensor, obtained using our previous model, against the ground truth provided by load cells placed along the environment.

5.1 Experimental Setup

A tendon-driven robot with a diameter of 12 mm was designed and fabricated for the demonstration. The robot is made of a flexible backbone, and consists of two sections, each containing a set of 16 disks equally spaced 1 cm apart along the backbone. Two sets of 3 tendons are routed along the length of the backbone and used to actuate each segment with motors at the base of the robot. The final design of the tendon-driven robot is shown in Fig. 5.1.

In order to attach a sensor to a disk along the length of the robot, a mounting plate was

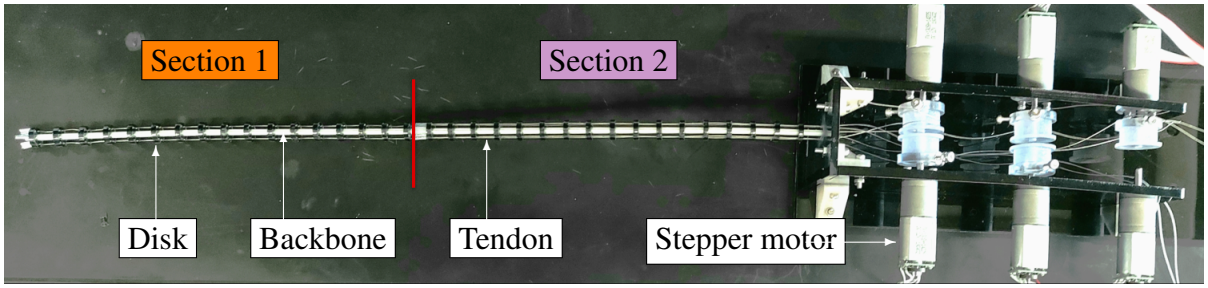

Figure 5.1. Picture of the designed tendon-driven robot.

designed, and the back side of the PCB was rigidly attached via adhesive to the mounting plate as shown in Fig. 5.2.

Each PCB was connected to a VNA port with a U.FL cable in order to both excite the sensor with a 900 MHz signal and to measure the phase shift induced by the deformation. For this demonstration, two sensors (sensor 1 and sensor 2) were mounted to the robot, one on each section, facing opposite directions. The final placement of the sensors on a tendon-driven robot for demonstration is presented in Fig. 5.3.

The robot was actuated with the stepper motors controlling the tension of tendons to achieve three different configurations. For each configuration, the force sensors hit a corresponding 'obstacle' in the environment. To assess the performance of the sensors in this more realistic use case, load cells were used as the designated environment 'obstacles', and these measurements were used as the ground-truth forces. For three different robot configurations, the force sensors and environmental 'obstacles' interacted, and their placements are shown in Fig. 5.4. For each sensor, 10 readings were collected and averaged for each of the three

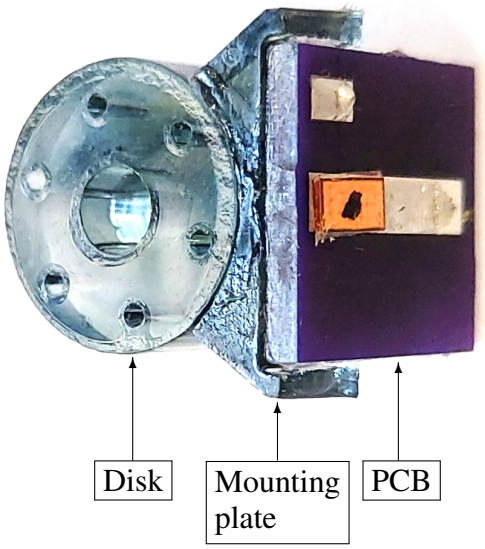

Figure 5.2. Picture of the PCB attached to the disk with a designed mounting plate.

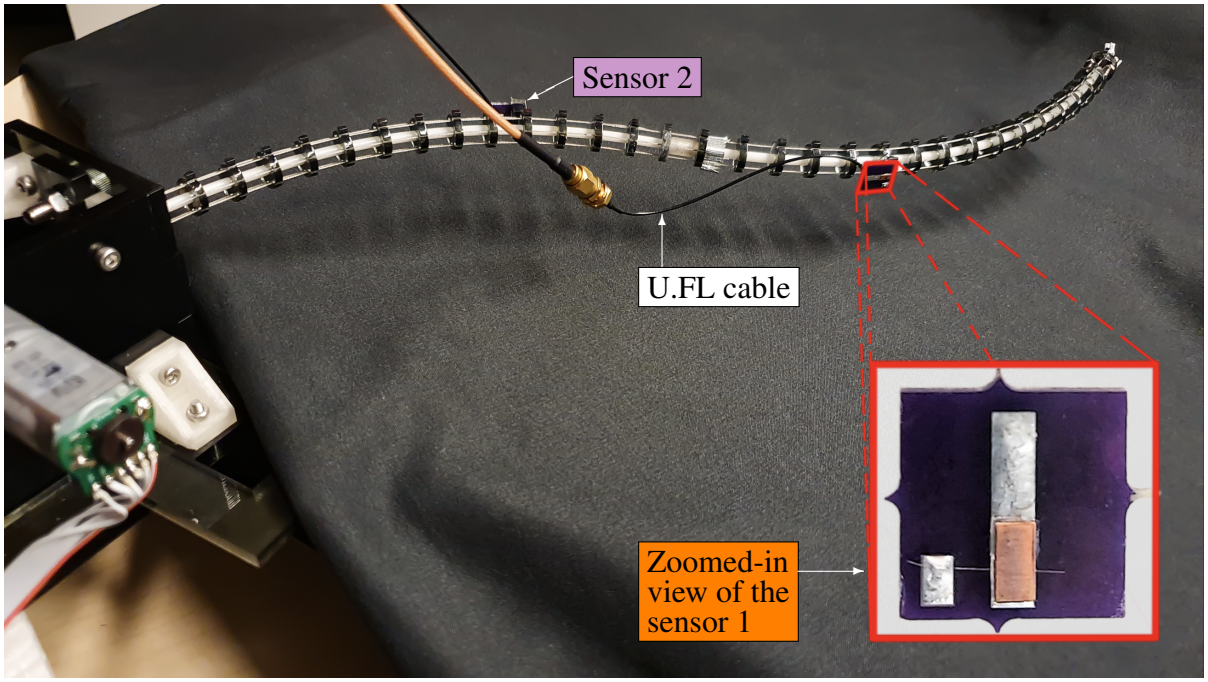

Figure 5.3. Picture of the proposed force sensors assembled on a tendon-driven robot, with a close-up view of the sensor 1 in the bottom right corner.

configurations. The models created in Section 4.2 were then used to calculate the force outputs from the sensors, and these values were compared to the ground-truth force readings from the load cells.

5.2 Experimental Results

The three different robot configurations for which the sensors were evaluated are visible in the first row of Table 5.1. These configurations were selected to demonstrate different levels of force interactions between the sensor and its environment, increasing from the left to the right.

These shapes enabled forces of different magnitudes to be applied to our sensors, thus allowing us to validate our sensors across a wide force range. The estimated force magnitudes applied to the sensors are visible in the bottom row of the Table. 5.1. The RMS error for sensor 1 and 2 across the three different robot configurations assessed are 0.17 N and 0.31 N,

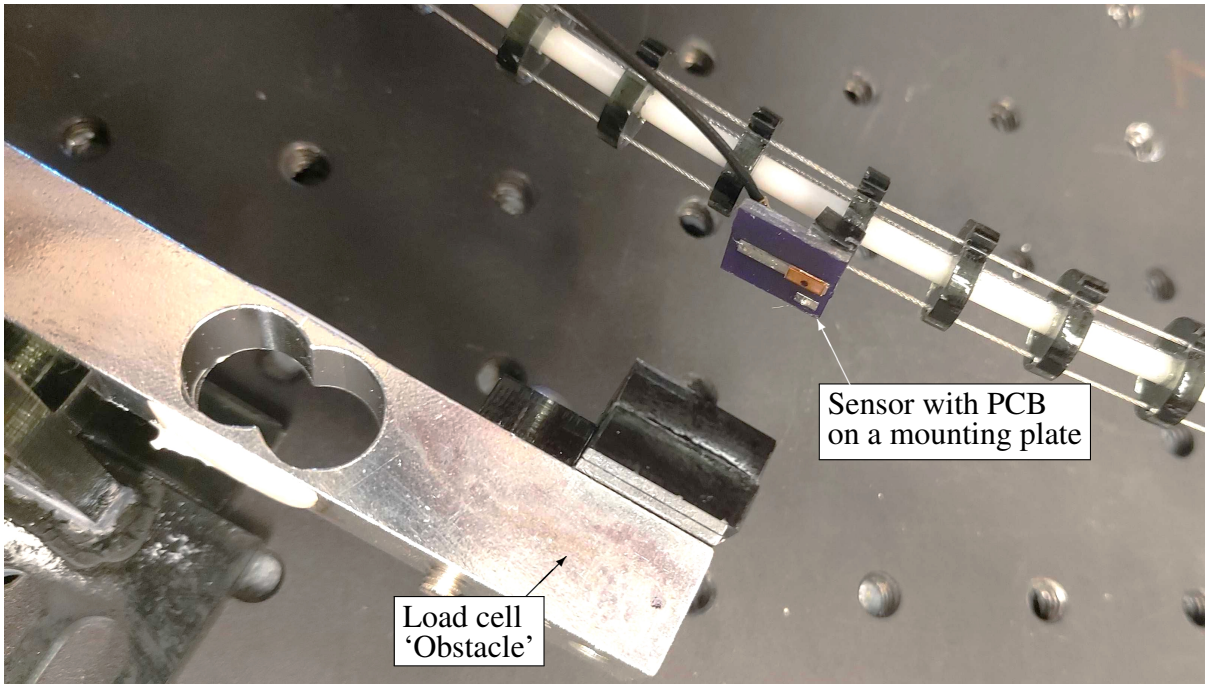

Figure 5.4. Picture of the fabricated sensor with PCB attached to the tendon-driven interacting with a load cell.

which is in accordance with the experimental model validated in Section 4.2. The slightly higher RMS error shown by sensor 2 may have been due to non-uniform loading or shear forces, which are not considered when modeling the sensor. However, even with the current RMS error levels, the sensors have a high enough resolution and accuracy to provide multiple intermediate measurements between the upper and lower thresholds of applied forces during surgical operations, as seen by examining the required force ranges proposed for many different types of surgeries [11, 12, 50]. This information could help surgeons apply an acceptable range of forces to improve safety and prevent injury during surgical procedures. Thus, these results are satisfying and tend to show the performance and benefit of our proposed sensor in a more realistic use case.

Table 5.1. Robot configurations were selected to demonstrate our force sensors, with an estimation of the force using our sensor model overlaid with the ground truth force measurement provided by the load cells.

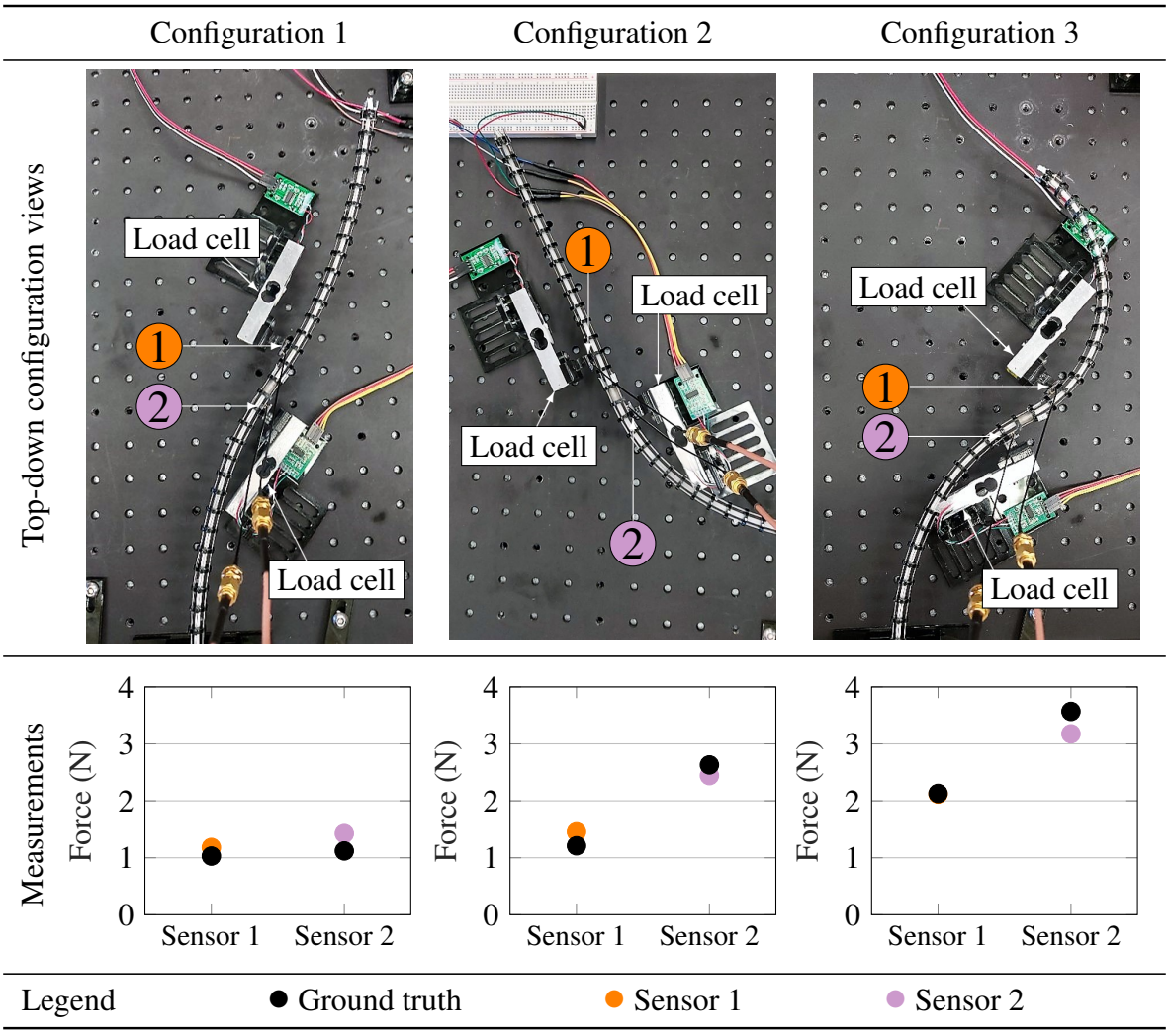

Chapter 6

Sensor Interface Advances and Evaluations

In the previous chapters, the PCB used for test purposes had a relatively large size compared to that of the sensor; thus, its size dictated the overall size. Further, the rigid PCB required additional support for reliable mounting on curved surfaces of continuum robots. Therefore, in this chapter, we propose a more practical sensor interface that is flexible, wireless, and battery-free. These properties significantly increase the suitability of the sensors for medical applications. Then, the sensor performance with different interfaces is evaluated to validate its adequacy.

6.1 Flexible PCB

We start by interfacing the sensor with a flexible PCB and evaluate the overall system performance on a curved surface. The flexible PCB was fabricated (11.557mm $\times$ 11.684mm $\times$ 0.102mm) and attached to a disk ($D = 12$ mm), as shown in Fig. 6.1a.

The soldering process for integrating the sensor with the rigid PCB was a challenge in Section 4.2, and it was even more challenging to solder the sensor to a curved PCB. The difficulties in this process include: ensuring full contact between the sensor and the flexible PCB without any gaps and preventing the solder from contacting the polymer as it might change the sensor capacitance or cause a short. Therefore, some adjustments were made in the sensor

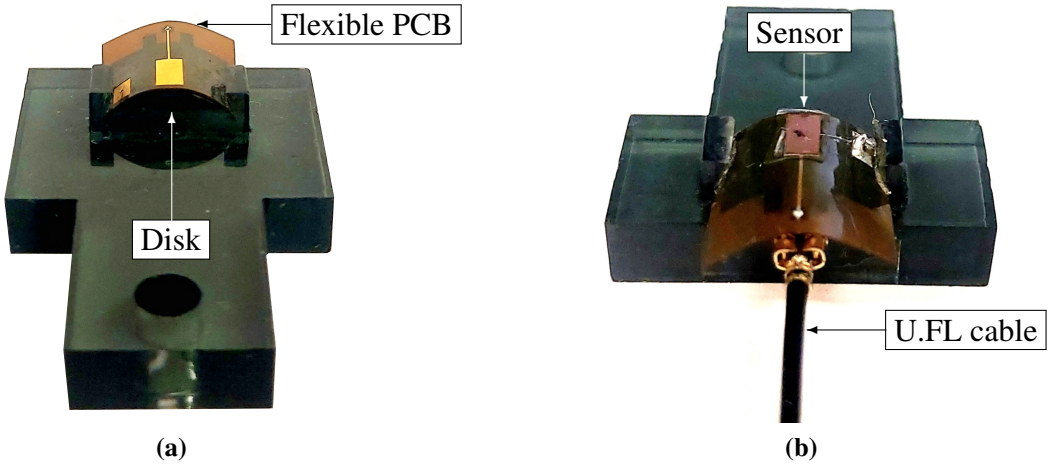

Figure 6.1. Photos of the final sensor integrated with the flexible PCB, with (a) flexible PCB attached to a disk and (b) sensor integrated with the flexible PCB.

fabrication and integration process to ease the sensor integration with the flexible PCB. The bottom copper layer of the sensor was removed and replaced with a copper microstrip of the flexible PCB to ease the sensor integration steps, as illustrated in Fig. 6.2.

This replacement of the bottom copper layer removed the need for soldering since the improved adhesion from the UVO treatment between the microstrip line of the flexible PCB and the bottom surface of the polymer was enough to hold the sensor under an applied force rigidly. The sensor design is still capacitive since the microstrip line is made with copper and acts as the bottom conductive copper layer of the original sensor. The sensor attached to the flexible PCB

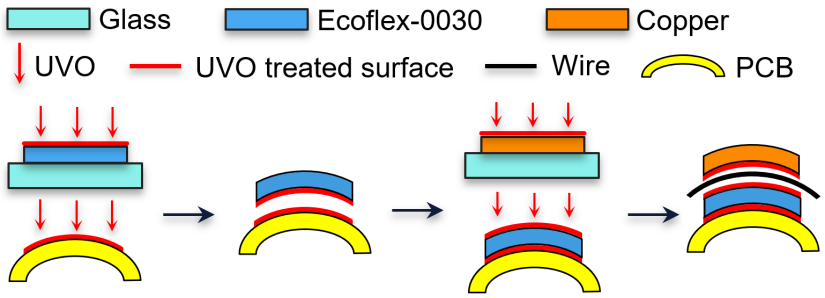

Figure 6.2. Illustration of the fabrication and integration steps for the sensor to the flexible PCB.

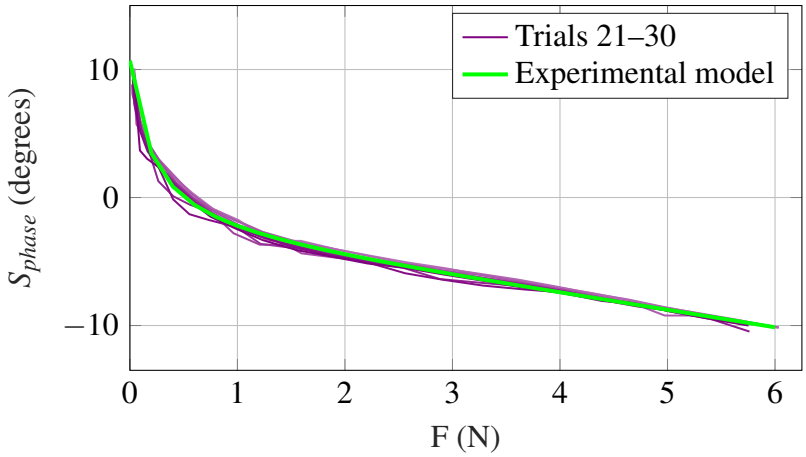

Figure 6.3. The plot of the experimental results with the sensor on a flexible PCB for trials 21 to 30, along with the model created from the experimental data.

is shown in Fig. 6.1b. Next, the flexible PCB was connected to VNA via a U.FL cable to read the reflected signals. Then, the sensor evaluation was performed under the same experimental settings as described in Section 4.1. The experimental results of a sensor mounted on a flexible PCB are shown in Fig. 6.3.

Similar to Section 4.2, a model was then computed to estimate the force for a measured phase and evaluate the sensor performance. A 3$^{\text{rd}}$ order rational was used to curve fit the results and is given by,

$$F(S_{phase}) = \frac{p_1 S_{phase}^3 + p_2 S_{phase}^2 + p_3 S_{phase} + p_4}{S_{phase}^2 + q_1 S_{phase} + q_2}, \tag{6.1}$$

where the coefficients used for the sensor model are given in Table 6.1.

Table 6.1. Corresponding coefficients of the experimental model for the sensor with flexible PCB.

Coefficients	p_1	p_2	p_3	p_4	q_1	q_2
S_{phase}	-0.1027	1.113	-7.094	52.45	14.47	103.4

The sensor model is also shown in green in Fig. 6.3 and show a qualitatively good

Table 6.2. Sensitivity and resolution of the sensor on a flexible PCB

Force range	0 - 0.5 N		0.5 - 6 N	
Metric	Sensitivity	Resolution	Sensitivity	Resolution
Sensor	18.57 °/N	0.54 mN	1.93 °/N	5.20 mN

fit with the RMS error of 0.12 N between the experimental model and the experimental data. Additionally, the full scale output the sensor is 19.88 °. From the sensor model and the sensor's full scale output, the sensor's sensitivity and resolution were also evaluated in Table 6.2.

As shown in Table 6.2, the sensitivity and the resolution for the sensor with the flexible PCB were 18.57 °/N and 0.54 mN for 0-0.5 N, and 1.93 °/N and 5.20 mN for 0.5-6 N. There are some deviations in the sensitivity and resolution results compared to Section 4.2. However, the sensor can still reliably resolve forces over 0.05 N for the entire force range, which is close enough to our targeted force measure range of 0.04 N to 6 N. These differences in the sensitivity and resolution could have occurred from the slight change in the sensor geometry due to the curvature of the flexible PCB and the replacement of the bottom copper layer to the microstrip line of the flexible PCB, which could have a different thickness. Overall, the main improvement in interfacing the sensor with a flexible PCB is that it enables the sensor to be placed on curved surfaces, which is one of the main characteristics of most surgical tools.

6.2 Wireless PCB

Now that the sensor performance and suitability on a curved surface are verified, we interface the sensor with a rigid PCB and Radio Frequency Identification Integrated Circuit (RFID IC) to check its performance in a wireless environment.

For the wireless operation of the sensor, the RFID reader antenna (ALR-8698, Alien Technology) is used as a reflected signal measuring instrument. It is important to note that in a wireless operation, the reflected signal from the sensor has to be modulated to isolate the

sensor's signal reflection from the various reflections from its neighboring environment for accurate signal readings. Therefore, the RFID IC needs to be placed where it would modulate the phase-shifted signal before its reflection to the RFID reader antenna. In order to modulate the reflected signal, the sensor needs to pass through the signal instead of just reflecting it. This is because the existing backscatter modulation ICs implement both energy harvesting units and modulation blocks and are designed to reflect the modulated signal. Therefore, to reflect the signal from the RFID IC, the sensor has to be placed between the RFID reader antenna and the RFID IC. However, we need to confirm if the signal reflects as soon as it reaches the sensor or passes through the sensor and reflects at the end of the microstrip line as it travels along the signal trace. In order to check the signal reflection point, the simulation design in Section 2.2 was slightly modified. The microstrip line of the PCB is fully extended to the end of the PCB, and a 2nd port was assigned at the end to receive signals that pass through the sensor as shown in Fig. 6.4.

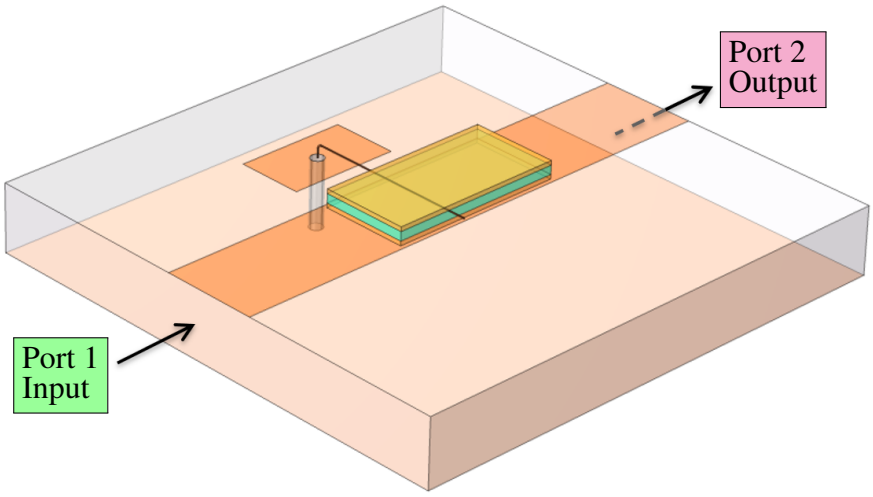

Figure 6.4. COMSOL simulation model of the sensor with PCB connected to two ports.

Then, with the same range of force, 0 N to 6 N, the range of S_{11} (single port reflection

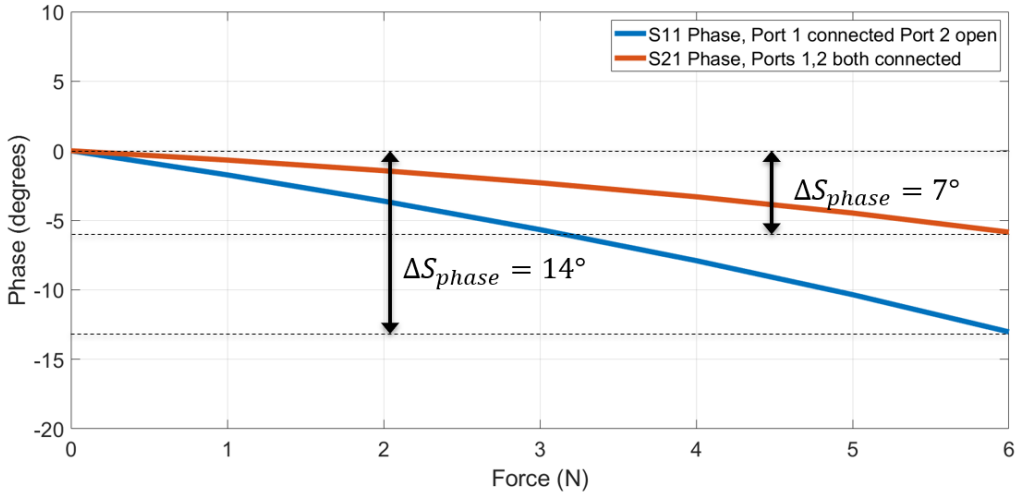

Figure 6.5. The range of S_{phase} doubled in a single port simulation than that of the two-port.

phase) and S_{21} (two-port pass through phase) phase was computed. From the results presented in Fig. 6.5, it is observed that the total phase shift was around 7 ° and 14 ° for single port and two ports, respectively.

Therefore, we conclude that the input signal passes through the sensor and reflects at the end of the microstrip line since the total phase shift doubled in the single port case compared to that of the two-port case. In other words, the phase of the signal shifts as it passes through the sensor. Since the signal reflection happens after the signal passes through the sensor, the RFID IC was placed after the sensor. The sensor was therefore located between the antenna and the RFID IC. The RFID IC and the sensor were then soldered onto the rigid PCB. Lastly, the dipole antenna was connected to the rigid PCB via a U.FL cable for wireless communication. The final fabricated wireless PCB with the sensor is shown in Fig. 6.6.

To read the signal from the antenna, the RFID antenna reader was placed above the benchtop setup, as shown in Fig. 6.7.

Then, the sensor evaluation was performed under the same experimental settings as

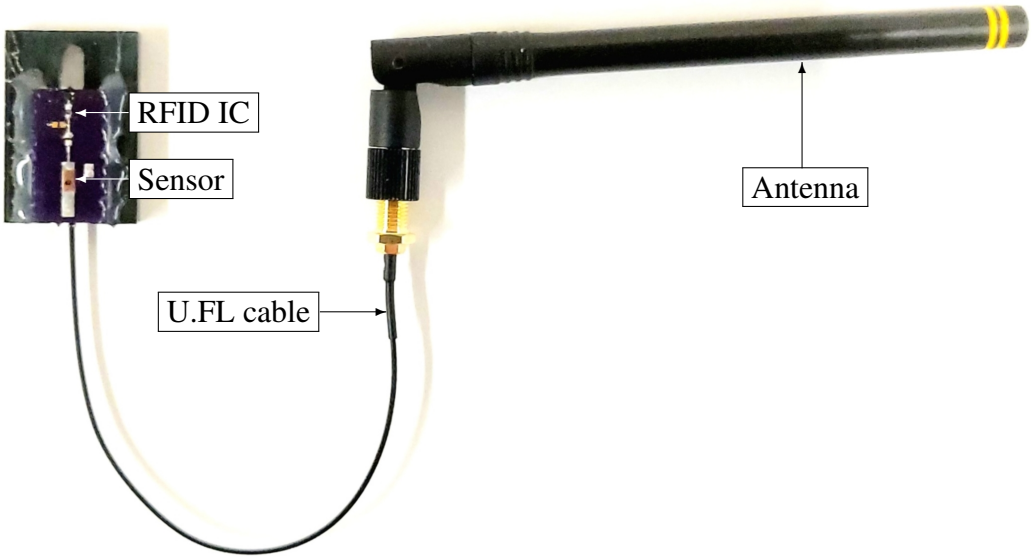

Figure 6.6. Final fabricated sensor and PCB connected to RFID IC and antenna for wireless communication.

described in Section 4.1. However, since each reading from the wireless communication results in an averaging error, every level of force applied to the sensor started from 0 N. To be more specific, the reflected signal modulated from the RFID IC needs to be decoded via the RFID reader antenna to relate the phase shift readings to the applied force. When the RFID reader antenna receives the signal, the Electronic Product Code (EPC) ID information in the signal is used to identify the sensor signal from other signals from its neighboring environment. Then, the RFID reader antenna observes the channel estimates of the particular tag from the EPC ID and calculates phase shifts, leading to force estimation. When the RFID reader antenna estimates the phase shifts, it changes its frequency every 200 ms to avoid interference with other readers in the neighboring environment. This change in frequencies creates a random phase offset, leading to an additional phase shift in the phase calculations. Therefore, the channel index from the RFID reader antenna is used to isolate the phase shifts from each channel to compute the applied force estimation separately in each channel. These phase shifts across 50

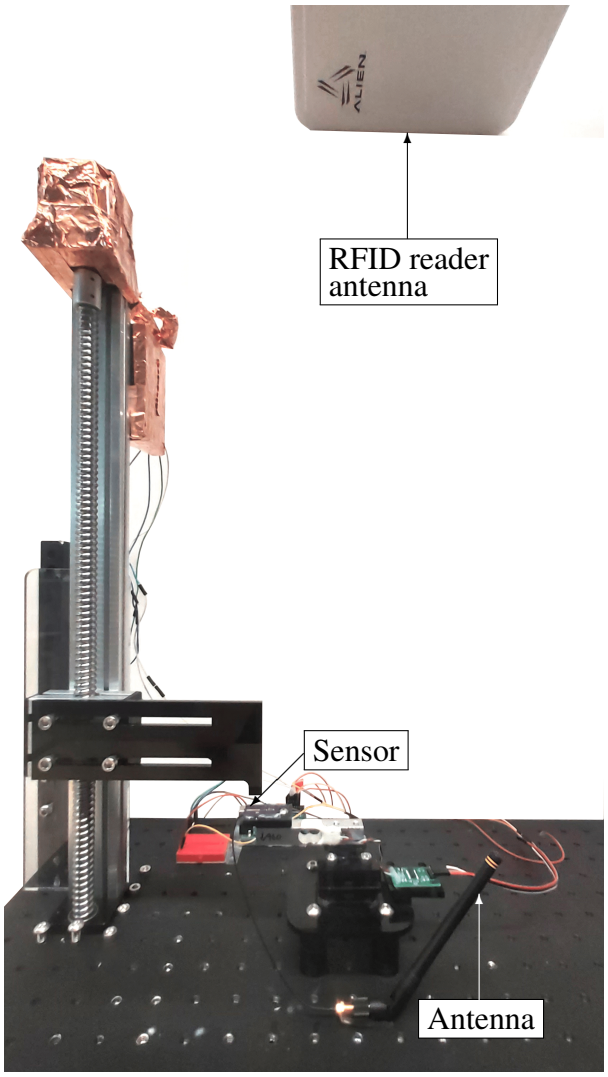

Figure 6.7. Final benchtop setting for a wireless communication

RFID channels in the RFID IC are then averaged between 900 MHz to 930 MHz to finalize the phase shift used for the force estimation. This averaging mechanism helps the sensor be robust to multipath signals in dynamic environments, where the signal could arrive at a receiver via two or more routes, since the multipath phase shifts averages to near zero. Therefore, because of the averaging error in this phase shift calculation process, the force applied to the sensor had to return back to 0 N before applying a new force and read a new phase shift to remove the accumulation of the averaging error (i.e. 0 N $\rightarrow$ 0.2 N $\rightarrow$ 0 N $\rightarrow$ 0.4 N $\rightarrow$ 0 N $\rightarrow$ 0.6 N $\rightarrow$ ...). The experimental results of a sensor interfaced with a wireless PCB are shown in Fig. 6.8.

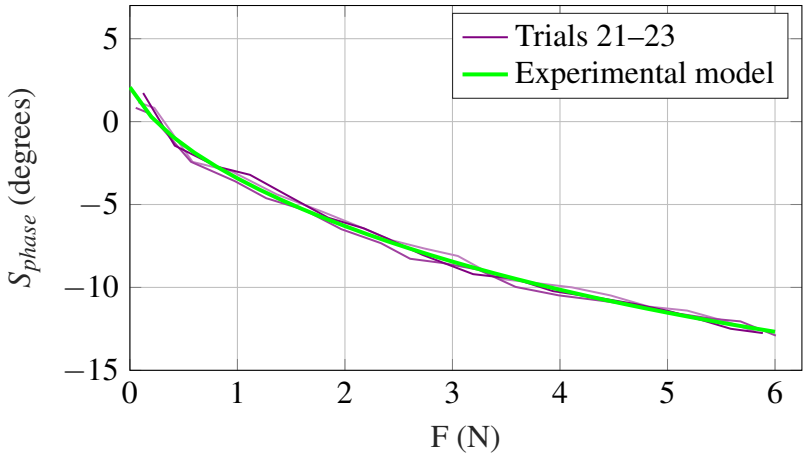

Figure 6.8. Plot of the experimental results with the sensor on a wireless PCB for trials 21 to 23 and the model created from the experimental data.

The curve fitted model of the sensor results is given by,

$$F(S_{phase}) = \frac{p_1 S_{phase}^3 + p_2 S_{phase}^2 + p_3 S_{phase} + p_4}{S_{phase}^2 + q_1 S_{phase} + q_2}, \tag{6.2}$$

where the coefficients used for the sensor model are given in Table 6.3.

The RMS error between the experimental model and the experimental data shown in Fig. 6.8 is 0.15 N. Using the constructed sensor model, the sensor's full scale output was 14.83 °. From our wireless experiments [31], it was observed that the phase averaging gives the phase resolution around 0.5 ° in a static environment and 0.8 ° to 1 ° in a dynamic environment. Since the sensor is highly likely to be in a dynamic environment when used for surgical processes, 1 ° wireless communication resolution was used to obtain the sensitivity and resolution of the tested sensor shown in Table 6.4.

Table 6.3. Corresponding coefficients of the experimental model for the sensor with wireless PCB.

Coefficients	p_1	p_2	p_3	p_4	q_1	q_2
S_{phase}	-6.143	381.6	-4675	8097	562.3	30780

Table 6.4. Sensitivity and resolution of the sensor on a wireless PCB

Force range	0 - 0.5 N		0.5 - 6 N	
Metric	Sensitivity	Resolution	Sensitivity	Resolution
Sensor	6.80 °/N	0.15 N	2.08 °/N	0.48 N

As shown in Table 6.4, the sensitivity and resolution for the sensor with wireless PCB were 6.80 °/N and 0.15 N for 0-0.5 N, and 2.08 °/N and 0.48 N for 0.5-6 N. There are some discrepancies in the sensor performance in the wired and wireless testing environment. This difference in sensor performance is mainly due to the resolution of the testing environment (0.01 ° for VNA and 1 ° for wireless communication), which decreases the sensor resolution in a wireless environment by 100 times compared to testing in a wired environment. Additionally, the full scale output and sensitivity differences could have occurred from the fabrication and integration process, which involves multiple manual steps. The sensor performance showed that the sensor is still valid in the wireless environment, and it can be used for specific surgical procedures discussed in Section 2.2. The main significance of adding the RFID IC to the sensor interface is making the whole sensor wireless and battery-free with the embedded energy harvesting feature in the RFID IC.

6.3 Flexible Printed Antenna

Now that the sensor is shown to work both on a curved surface and in a wireless environment, we propose a sensor interface that is both flexible and wireless. Here, we utilize the commercially available RFID sticker tag shown in Fig. 6.9, which already has a printed antenna connected to the RFID IC and is much more flexible than the flexible PCB from Section 6.1.

To interface the sensor with the RFID IC without a microstrip line, the sensor had to be directly connected to both sides of the RFID IC. Therefore, a few changes were made in the

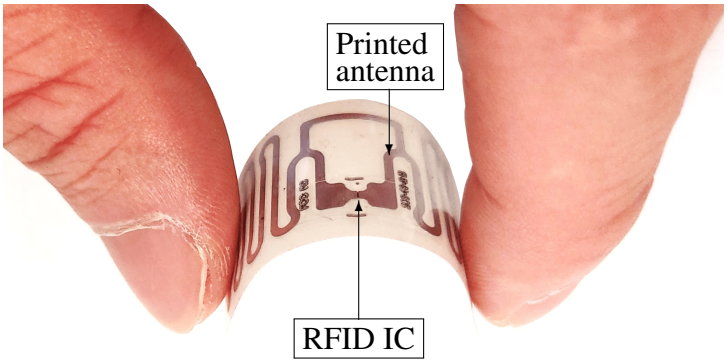

Figure 6.9. Flexible printed antenna with RFID IC used for the new interface.

sensor fabrication and integration process.

First, because each copper layer of the sensor had to be connected to the RFID, additional tungsten wire was added between the copper and Ecoflex 00-30 layer during the fabrication process, as shown in Fig. 6.10. Next, the RFID IC and its covering sheet, which is highlighted in yellow in Fig. 6.11a, were carefully removed using a knife. The sensor was attached to the top surface of the flexible printed antenna with a double-sided tape. Then, each tungsten wire from the sensor was placed between each side of the RFID IC sticker and the printed antenna and was firmly pressed for a solid connection. The interface design and final fabricated sensor interfacing with the commercial RFID sticker are shown in Fig. 6.11a and 6.11b.

The sensor performance was tested in the same environment setting as Section 6.2. The

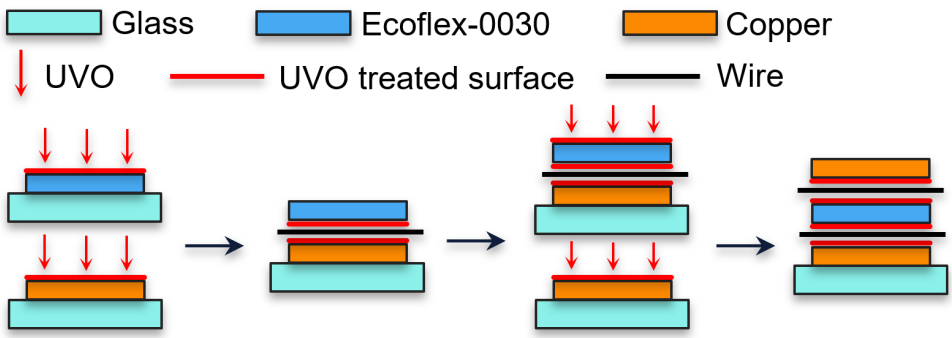

Figure 6.10. Illustration of the sensor fabrication steps for the interface with the flexible printed antenna.

(a) (b)

Figure 6.11. Photos of the flexible printed antenna, with (a) a representation of the sensor and wires overlaid on top, and (b) the actual sensor once integrated.

results are shown in Fig. 6.12.

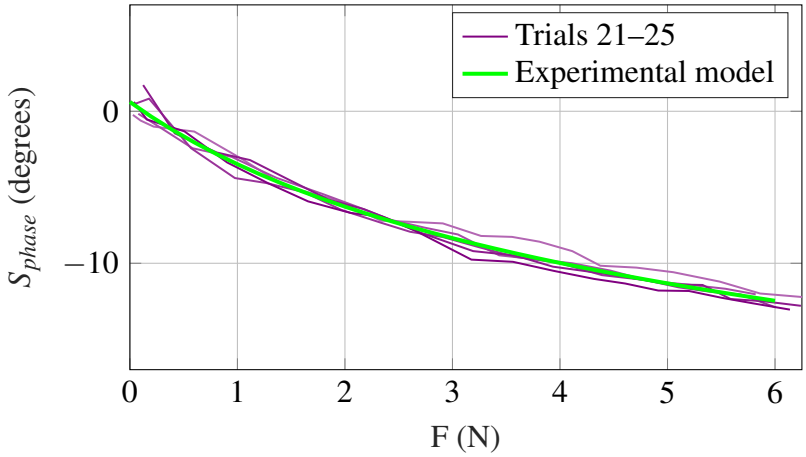

Figure 6.12. Plot of the experimental results with the sensor on a flexible printed antenna for trials 21 to 25, along with the model created from the experimental data.

The curve fitted model of the experimental results is given by,

$$F(S_{phase}) = \frac{p_1 S_{phase}^2 + p_2 S_{phase} + p_3}{S_{phase}^2 + q_1 S_{phase} + q_2}, \tag{6.3}$$

where the coefficients used for the sensor model is given in Table 6.5.

The sensor model in Fig. 6.12 has an RMS error between the experimental model and the experimental data of 0.26 N. The full scale output of the sensor is 13.76 ° for the entire

Table 6.5. Corresponding coefficients of the experimental model for the sensor with a flexible printed antenna.

Coefficients	p_1	p_2	p_3	q_1	q_2
S_{phase}	1862	-16120	15580	1255	102000

range of forces. Similar to Section 6.2, the sensitivity and resolution of the sensor were also evaluated considering the wireless communication resolution of 1 ° with the sensor model as shown in Table 6.6.

As shown in Table 6.6, the sensitivity and resolution for the sensor with flexible printed antenna were 5.75 °/N and 0.17 N for 0-0.5 N, and 1.98 °/N and 0.51 N for 0.5-6 N. The sensor performance is slightly degraded compared to the results with the wireless PCB in Section 6.2. This could be due to the loss of rigidity in the sensor placement. The sensor was attached using a double-sided tape, which could have a small amount of elasticity causing errors in measuring the applied force. The sensor performance evaluation on a flexible printed antenna showed that both flexible and wireless functions could be added to the sensor interface without affecting each other.

6.4 Flexible and Wireless PCB

The second flexible and wireless interface is connecting the sensor to a flexible PCB with a flexible spiral antenna. This new interface is composed of two parts: the spiral antenna and the PCB which are shown in Fig. 6.13a. First, the flexible PCB was soldered to the bottom

Table 6.6. Sensitivity and resolution of the sensor on a flexible printed antenna

Force range	0 - 0.5 N		0.5 - 6 N	
Metric	Sensitivity	Resolution	Sensitivity	Resolution
Sensor	5.75 °/N	0.17 N	1.98 °/N	0.51 N

copper section of the spiral antenna. The final interface has dimensions of 10 mm $\times$ 12.20 mm $\times$ 0.102 mm. Next, the sensor and the RFID IC was soldered on a microstrip line of the flexible PCB. The final sensor integration is shown in Fig. 6.13b.

The sensor performance was tested in the same environment setting as Section 6.2. The results are shown in Fig. 6.14.

The curve fitted model of the experimental results is given by,

$$F(S_{phase}) = \frac{p_1 S_{phase}^3 + p_2 S_{phase}^2 + p_3 S_{phase} + p_4}{S_{phase}^2 + q_1 S_{phase} + q_2}, \tag{6.4}$$

where the coefficients used for the sensor model is given in Table 6.7.

Table 6.7. Corresponding coefficients of the experimental model for the sensor with a flexible and wireless PCB.

Coefficients	p_1	p_2	p_3	p_4	q_1	q_2
S_{phase}	-0.5597	-2.589	-4.368	3.177	4.771	8.971

The sensor model in Fig. 6.14 has an RMS error between the experimental model and the experimental data of 0.22 N. The full scale output of the sensor is 11.11 ° for the entire range of forces. Similar to Section 6.2, the sensitivity and resolution of the sensor were also

(a) **(b)**

Figure 6.13. Photos of the final flexible and wireless PCB, with (a) the design of the flexible PCB on the left and the spiral antenna on the right, and (b) interfaced with the RFID IC and the sensor.

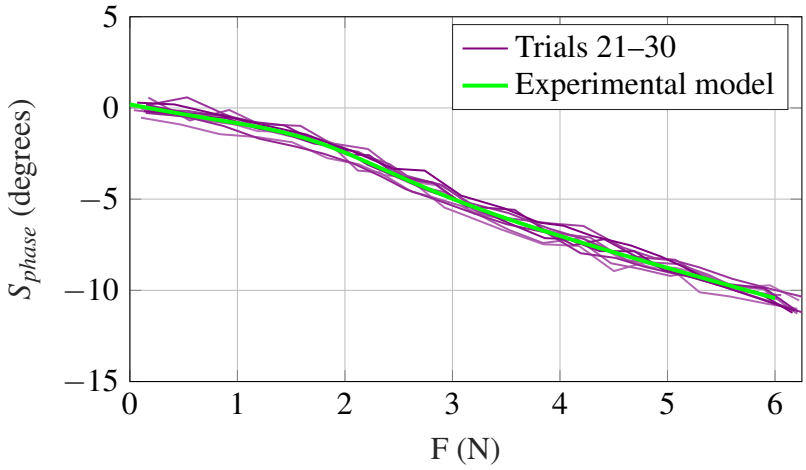

Figure 6.14. Plot of the experimental results with the sensor on a flexible and wireless PCB for trials 21 to 30, along with the model created from the experimental data.

evaluated considering the wireless communication resolution of 1 ° with the sensor model as shown in Table 6.8.

Table 6.8. Sensitivity and resolution of the sensor on a flexible and wireless PCB

Force range	0 - 0.5 N		0.5 - 6 N	
Metric	Sensitivity	Resolution	Sensitivity	Resolution
Sensor	1.49 °/N	0.67 N	1.88 °/N	0.53 N

As shown in Table 6.8, the sensitivity and resolution for the sensor with flexible printed antenna were 1.49 °/N and 0.67 N for 0-0.5 N, and 1.88 °/N and 0.53 N for 0.5-6 N. The sensor performance is slightly degraded compared to the results with the wireless PCB in Section 6.2 and the flexible printed antenna in Section 6.3. This could be due to the miniaturization of the antenna, which could have lower wireless communication quality. Finally, with the new sensor interface, the sensor performance showed its suitability both in flexible and wireless environment.

Chapter 7

Wireless Communication Evaluation

In the previous chapters, the sensor performance in various interfaces and environments was primarily evaluated. However, since the sensor output is received via wireless communication, the reliability test on this wireless communication in a more realistic environment also has to be evaluated. Also, the sensor's operating distance range needs to be tested for more practical use of the sensor in a real scenario.

7.1 Phantom Testing

The sensor performance was tested in the open air in the previous chapters. However, since the sensor is targeted for in-vivo surgical procedures, its performance in phantoms was first performed to evaluate its wireless communication quality in an in-vivo environment. The pork belly (approximately 4 cm thick) was used as a multi-layer tissue to mimic the human tissue. The size of the pork belly was big enough to cover the whole area between the sensor and the RFID reader antenna. With the experimental settings described in Section 6.2, the pork belly was additionally placed in a container between the RFID reader antenna and the sensor interfaced with the flexible printed antenna (Section 6.3), as shown in Fig. 7.1.

The phantom testing was performed with a sensor interface introduced in Section 6.3 in the same wireless settings described in Section 6.2 to observe the effect of the phantom on the sensor's performance. The experimental results are shown in Fig. 7.2.

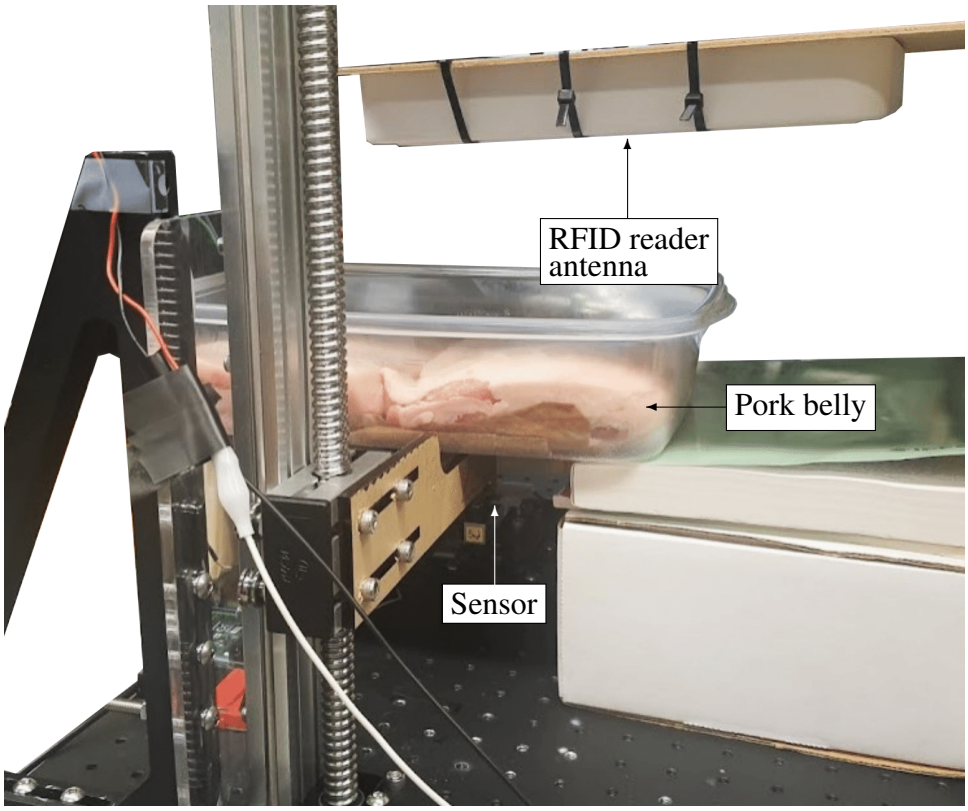

Figure 7.1. Experimental setup of the sensor with the phantom in a wireless environment.

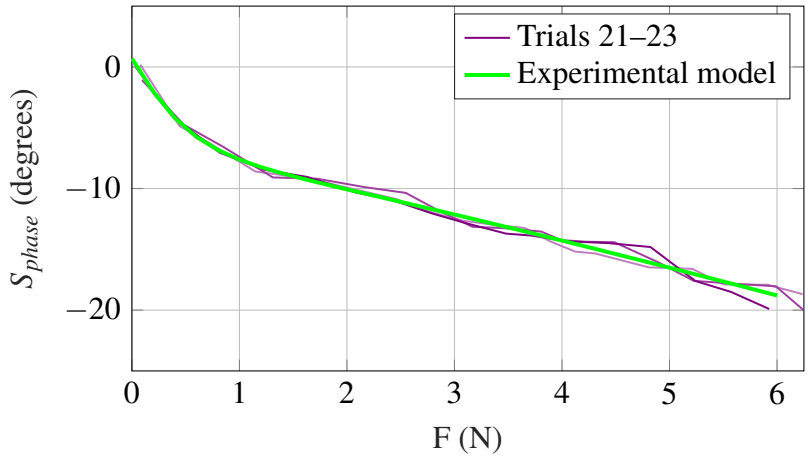

Figure 7.2. Plot of the experimental results with the sensor in the phantom environment for trials 21 to 23 and its experimental model.

The curve fitted model of the experimental results is given by,

$$F(S_{phase}) = \frac{p_1 S_{phase}^3 + p_2 S_{phase}^2 + p_3 S_{phase} + p_4}{S_{phase}^2 + q_1 S_{phase} + q_2}, \tag{7.1}$$

where the coefficients used for the sensor model are given in Table 7.1.

Table 7.1. Corresponding coefficients of the experimental model from the phantom test.

Coefficients	p_1	p_2	p_3	p_4	q_1	q_2
S_{phase}	0.1416	6.709	5.14	34.62	31.99	480.3

The sensor model in green in Fig. 7.2 has an RMS error of 0.21 N between the experimental model and the experimental data. Similarly, the full scale output of the sensor, 18.89 °, and the constructed sensor model were used to compute the sensitivity and resolution of the sensor with the wireless communication resolution of 1 ° and is shown in Table 7.2.

As shown in Table 7.2, the sensitivity and resolution for the sensor with flexible and wireless PCB were 9.77 °/N and 0.1 N for 0-0.5 N, and 2.55 °/N and 0.39 N for 0.5-6 N. The sensor performance was slightly improved in a phantom environment compared to the results in Section 6.3 without the phantom. This could be due to the presence of the phantom, which absorbs and blocks other signals from its neighboring environment leading to a decrease in averaging error. Therefore, the performance of the sensor in an actual use case in-vivo is expected to be even more promising since the sensor will not only be covered by the phantom on its top surface but also surrounded in every direction with the phantom, which could remove more signals that would degrade the quality of the wireless communication.

7.2 Wireless Range Testing

Next, the test on the operating distance range of the wireless communication between the sensor and the RFID reader antenna is conducted. This is important because the operating distance range of the sensor determines the placement of the RFID reader antenna and its

Table 7.2. Sensitivity and resolution of the sensor in a phantom environment

Force range	0 - 0.5 N		0.5 - 6 N	
Metric	Sensitivity	Resolution	Sensitivity	Resolution
Sensor	9.77 °/N	0.1 N	2.55 °/N	0.39 N

suitability for application for specific lengths of surgical instruments. The RFID reader antenna and the sensor with its interface from Section 6.3 were oriented vertically, and the distance between them was varied. Further, an additional flexible printed antenna without the sensor was examined along with the one with the sensor to observe the sensor's effect on the quality of wireless communication. The experimental setup is shown in Fig. 7.3.

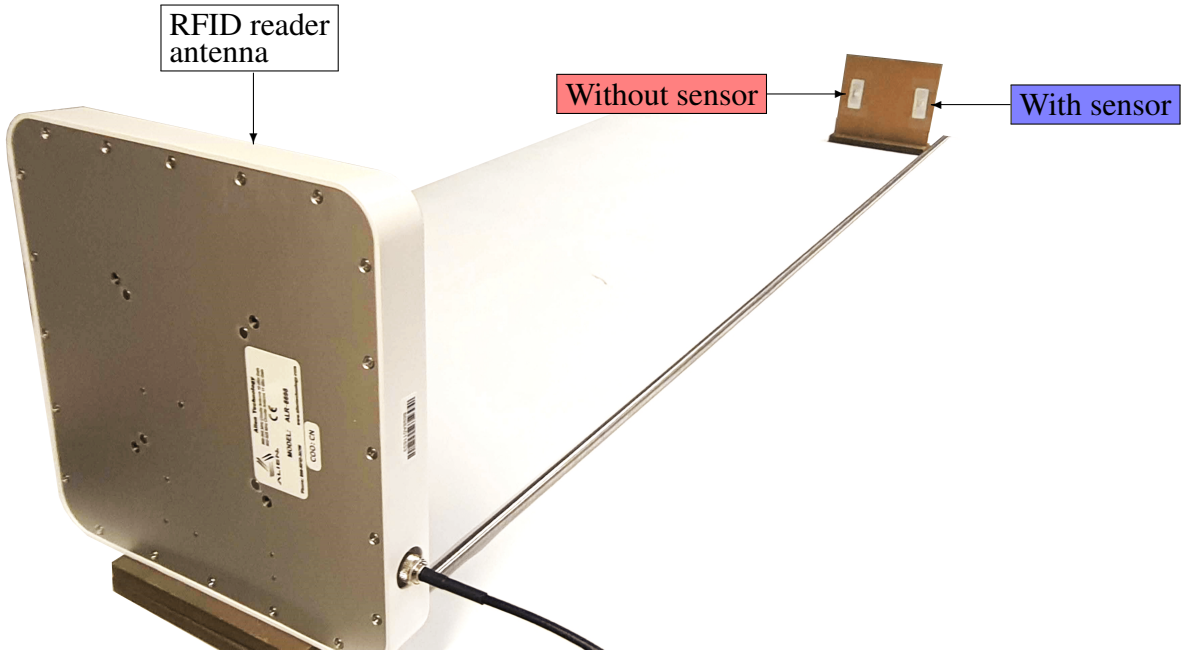

Figure 7.3. Experimental setup for the operating distance range of the sensor in a wireless environment.

The distance between the RFID reader antenna and the sensors increased from 0.5 m to 5 m with an increment of 0.2 m. The Received Signal Strength Indicator (RSSI), which indicates the strength of the received signal compared to the transmitted signal, was used as a

primary metric in determining the quality of wireless communication and the cut-off distance between the reader and the sensor. The cut-off threshold of the RSSI was set to -70 dBm, where wireless communication is considered unable to maintain a usable connection. The experimental results is shown in Fig. 7.4.

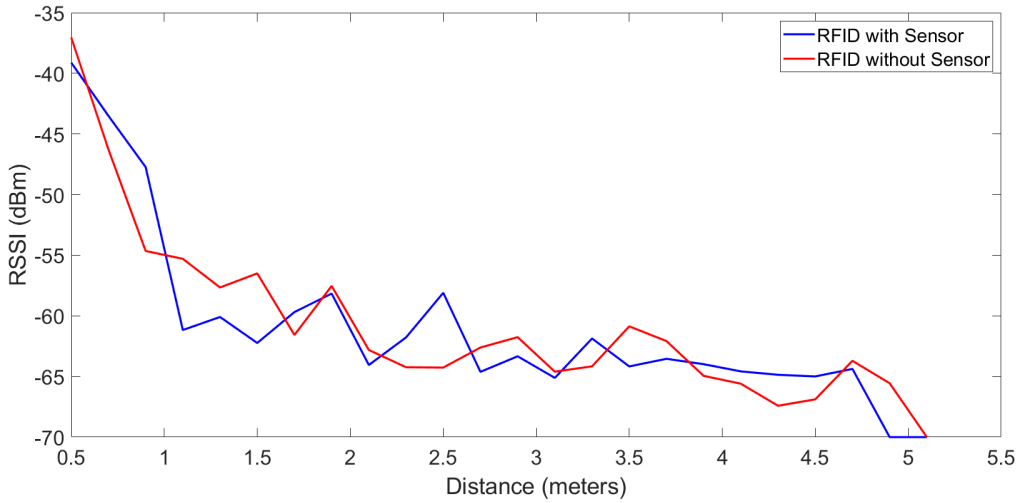

Figure 7.4. Experimental results for the operating distance range of the sensor in a wireless environment.

Overall, there was not much deviation between the two results in RSSI. The maximum working distance for the RFID with and without the sensor was 4.8 m and 5.2 m, respectively. This difference is relatively small compared to the overall working distance range of 4.3 m and 4.7 m for both cases. Therefore, the sensor's effect on the RSSI is minimal, making it possible to increase the operating distance range with the improvements only in the RFID reader antenna or the flexible printed antenna performance. The working range evaluated above is more than twice an average human height which would remove some constraints in the placement of the RFID reader antenna in a real scenario.

Chapter 8

Discussion and Future work

In this work, a new type of force sensor based on the principle of wave backscattering was presented. This sensor transduces an applied force into a change in the phase of a reflected electromagnetic wave, thus enabling compatibility with wireless interfaces. With a new working mechanism, the sensor design has been scaled down more than $1,000$ times compared to the previous design without affecting the sensor sensitivity and resolution. The proposed sensor was simulated using FEA and designed to enable the measurement of forces in the range of 0 N to 6 N. Two prototypes were fabricated and evaluated experimentally and showed phase shifts in accordance with those expected from the simulations. A model was then created for each of the two fabricated sensors based on the experimental data, and the constructed models were used to evaluate the sensor performance of each sensor. Next, the performance of the sensors was evaluated in an actual use case, where they were mounted on a continuum robot to measure contact forces with obstacles. The RMS error between the estimated forces and the ground truth measurements were 0.17 N and 0.31 N for sensors 1 and 2, respectively.

Next, different interfaces were tested with the sensor to improve its suitability for medical applications. With the flexible PCB, the sensor performance on a curved surface was evaluated, and the results showed its compatibility with surgical instruments with curved surfaces. Additionally, a wireless PCB was designed by adding an RFID component in the circuit to utilize the frequency response of the capacitive-based sensor and make the system wireless.

The sensor performance was evaluated with an RFID reader antenna in a wireless environment. The sensor's resolution in a wireless environment decreased due to the lower phase reading resolution in a dynamic wireless setting. Therefore, the lower resolution in force measurement resulted in increasing the minimum force that can be reliably resolved. The introduction of the RFID IC in the circuit enabled wireless and battery-free functions of the sensor. Further, the sensor interface with a flexible printed antenna that is both flexible and wireless was tested to confirm if both functions could be obtained simultaneously. The sensor performance is slightly degraded compared to that of the wireless PCB, which could be due to the miniaturization of the antenna. However, the sensor results were still repeatable, with its resolution as high as 0.17 N in this interface. In addition, a flexible and wireless PCB that is much smaller than the flexible printed antenna was also used to test the sensor's performance. There was some decrease in the sensor's performance which could be explained by the miniaturization of the antenna lowering the wireless communication resolution. Lastly, the wireless communication quality was evaluated through a phantom model, and its reliable working distance was tested. The wireless communication was slightly better with the phantom, which could be explained by the characteristics of the tissue that absorb and block signals and noise from its neighboring environment. This is even more promising in a more realistic case where the tissue will not only be covering one side of the sensor but every side will be surrounded by the tissue, which could result in more accurate readings. The maximum distance in the wireless communication with the flexible printed antenna with the sensor was around 5 m, which makes the placement of the RFID reader antenna easier and gives more options for the placement of the sensor on a surgical instrument. It was observed that the sensor had little effect on the RSSI, which means that the sensor performance could be further improved with better wireless communication equipment.

Our next step will be to miniaturize the sensor and its interface further. Miniaturizing the sensor is possible based on the analysis performed with our multiphysics model. Better equipment improvements in the fabrication process could enable sensor fabrication with optimal

dimensions which is smaller than the ones used in this work. The PCB and the printed antenna dimensions were mainly chosen for implementation convenience and were not optimized. Therefore, the PCB and printed antenna dimensions will be reduced for better integration with robotic systems. In addition, the sensor and its interface will be hermetically sealed to make them biocompatible, which is another essential factor when used for surgical procedures. Further, the integration of multiple sensors on a single flexible PCB will be explored since the current versions still have a relatively large interface for a single sensor. Enabling multiple sensors on a single interface would wrap the sensors around the circumference of a robot, resulting in high-density sensing on the surface of continuum robots. Lastly, an additional axis of force measurement will be added to also measure shear forces by adjusting the sensor design, for example, utilizing a differential capacitive sensor design.

This thesis, in part, has been submitted for publication of the material as it may appear in IEEE Robotics and Automation Letters, 2022, Park, Daegue; Gupta, Agrim; Bashar, Shayaun; Girerd, Cédric; Bharadia, Dinesh; Morimoto, Tania K., and Proceedings of the ACM on Interactive, Mobile Wearable and Ubiquitous Technologies, 2022, Gupta Agrim; Park, Daegue; Bashar, Shayaun; Girerd, Cédric; Morimoto, Tania K.; Bharadia, Dinesh. The thesis author was the primary author and co-author of these papers, respectively.

Bibliography

[1] L. S. Gan, K. Zareinia, S. Lama, Y. Maddahi, F. W. Yang, and G. R. Sutherland, "Quantification of forces during a neurosurgical procedure: a pilot study," *World neurosurgery*, vol. 84, no. 2, pp. 537–548, 2015.

[2] B. Bell, S. Stankowski, B. Moser, V. Oliva, C. Stieger, L.-P. Nolte, M. Caversaccio, and S. Weber, "Integrating optical fiber force sensors into microforceps for orl microsurgery," in *2010 Annual International Conference of the IEEE Engineering in Medicine and Biology*. IEEE, 2010, pp. 1848–1851.

[3] D. C. Rucker and R. J. Webster, "Deflection-based force sensing for continuum robots: A probabilistic approach," in *2011 IEEE/RSJ International Conference on Intelligent Robots and Systems*. IEEE, 2011, pp. 3764–3769.

[4] J. Konstantinova, A. Jiang, K. Althoefer, P. Dasgupta, and T. Nanayakkara, "Implementation of tactile sensing for palpation in robot-assisted minimally invasive surgery: A review," *IEEE Sensors Journal*, vol. 14, no. 8, pp. 2490–2501, 2014.

[5] P. Gallagher, L. Martin, L. Angel, and G. Tomassoni, "Initial clinical experience with cardiac resynchronization therapy utilizing a magnetic navigation system," *Journal of Cardiovascular Electrophysiology*, vol. 18, no. 2, pp. 174–180, 2007.

[6] F. Perna, E. K. Heist, S. B. Danik, C. D. Barrett, J. N. Ruskin, and M. Mansour, "Assessment of catheter tip contact force resulting in cardiac perforation in swine atria using force sensing technology," *Circulation: Arrhythmia and Electrophysiology*, vol. 4, no. 2, pp. 218–224, 2011.

[7] C. E. Reiley, T. Akinbiyi, D. Burschka, D. C. Chang, A. M. Okamura, and D. D. Yuh, "Effects of visual force feedback on robot-assisted surgical task performance," *The Journal of thoracic and cardiovascular surgery*, vol. 135, no. 1, pp. 196–202, 2008.

[8] G. Picod, A. Jambon, D. Vinatier, and P. Dubois, "What can the operator actually feel when performing a laparoscopy?" *Surgical Endoscopy and Other Interventional Techniques*, vol. 19, no. 1, pp. 95–100, 2005.

[9] B. Sümer, M. C. Özin, T. Eray, and İ. M. Koç, "The undamaged tissue grasping in a laparoscopic surgical grasper via distributed pressure measurement," *Tribology International*, vol. 113, pp. 330–337, 2017.

[10] T. Horeman, S. P. Rodrigues, J. J. van den Dobbelsteen, F.-W. Jansen, and J. Dankelman, "Visual force feedback in laparoscopic training," *Surgical endoscopy*, vol. 26, no. 1, pp. 242–248, 2012.

[11] B. K. Canales, D. Weiland, S. Reardon, and M. Monga, "Urethral catheter insertion forces: a comparison of experience and training," *International braz j urol*, vol. 35, pp. 84–89, 2009.

[12] R. N. Pedro, D. Weiland, S. Reardon, and M. Monga, "Ureteral access sheath insertion forces: implications for design and training," *Urological Research*, vol. 35, no. 2, pp. 107–109, 2007.

[13] K. S. Kaler, D. J. Lama, S. Safiullah, V. Cooper, Z. A. Valley, M. L. O'Leary, R. M. Patel, M. J. Klopfer, G.-P. Li, J. Landman, and R. V. Clayman, "Ureteral access sheath deployment: how much force is too much? initial studies with a novel ureteral access sheath force sensor in the porcine ureter," *Journal of endourology*, vol. 33, no. 9, pp. 712–718, 2019.

[14] R. D. D'Souza, A. Joshy, A. Mini, and N. M. Panicker, "The art of tactile sensing: a state of art survey," *Int. J. Sci. Basic Appl. Res*, vol. 26, pp. 252–266, 2016.

[15] Y. Al-Handarish, O. M. Omisore, T. Igbe, S. Han, H. Li, W. Du, J. Zhang, and L. Wang, "A survey of tactile-sensing systems and their applications in biomedical engineering," *Advances in Materials Science and Engineering*, vol. 2020, 2020.

[16] M. I. Tiwana, S. J. Redmond, and N. H. Lovell, "A review of tactile sensing technologies with applications in biomedical engineering," *Sensors and Actuators A: physical*, vol. 179, pp. 17–31, 2012.

[17] A. K. Golahmadi, D. Z. Khan, G. P. Mylonas, and H. J. Marcus, "Tool-tissue forces in surgery: A systematic review," *Annals of Medicine and Surgery*, vol. 65, p. 102268, 2021.

[18] R. Peña, M. J. Smith, N. P. Ontiveros, F. L. Hammond, and R. J. Wood, "Printing strain gauges on intuitive surgical da vinci robot end effectors," in *2018 IEEE/RSJ International Conference on Intelligent Robots and Systems (IROS)*. IEEE, 2018, pp. 806–812.

[19] B. Gil, B. Li, A. Gao, and G.-Z. Yang, "Miniaturized piezo force sensor for a medical catheter and implantable device," *ACS applied electronic materials*, vol. 2, no. 8, pp. 2669–2677, 2020.

[20] J. Heijmans, L. Cheng, and F. Wieringa, "Optical fiber sensors for medical applications—practical engineering considerations," in *4th European Conference of the International Federation for Medical and Biological Engineering*. Springer, 2009, pp. 2330–2334.

[21] D. Murzin, D. J. Mapps, K. Levada, V. Belyaev, A. Omelyanchik, L. Panina, and V. Rodionova, "Ultrasensitive magnetic field sensors for biomedical applications," *Sensors*, vol. 20, no. 6, p. 1569, 2020.

[22] H. Böse and E. Fuß, "Novel dielectric elastomer sensors for compression load detection," in *Electroactive Polymer Actuators and Devices (EAPAD) 2014*, vol. 9056. SPIE, 2014, pp. 232–244.

[23] K. Oliver-Butler, J. Till, and C. Rucker, "Continuum robot stiffness under external loads and prescribed tendon displacements," *IEEE Transactions on Robotics*, vol. 35, no. 2, pp. 403–419, 2019.

[24] C. Shi, X. Luo, P. Qi, T. Li, S. Song, Z. Najdovski, T. Fukuda, and H. Ren, "Shape sensing techniques for continuum robots in minimally invasive surgery: A survey," *IEEE Transactions on Biomedical Engineering*, vol. 64, no. 8, pp. 1665–1678, 2017.

[25] Q. Qiao, G. Borghesan, J. De Schutter, and E. Vander Poorten, "Force from shape—estimating the location and magnitude of the external force on flexible instruments," *IEEE Transactions on Robotics*, vol. 37, no. 5, pp. 1826–1833, 2021.

[26] T. Chen, Z. Saadatnia, J. Kim, T. Looi, J. Drake, E. Diller, and H. E. Naguib, "Novel, flexible, and ultrathin pressure feedback sensor for miniaturized intraventricular neurosurgery robotic tools," *IEEE Transactions on Industrial Electronics*, vol. 68, no. 5, pp. 4415–4425, 2020.

[27] A. J. DeRouin, B. D. Pereles, T. M. Sansom, P. Zang, and K. G. Ong, "A wireless inductive-capacitive resonant circuit sensor array for force monitoring," *Journal of Sensor Technology*, vol. 3, no. 03, p. 63, 2013.

[28] H. Li, J. Ding, S. Wei, B. Chu, L. Guan, L. Du, G. Liu, and J. He, "A miniature layered saw contact stress sensor for operation in cramped metallic slits," *Instruments and Experimental Techniques*, vol. 61, no. 4, pp. 610–617, 2018.

[29] X. Yi, T. Wu, Y. Wang, R. T. Leon, M. M. Tentzeris, and G. Lantz, "Passive wireless smart-skin sensor using rfid-based folded patch antennas," *International Journal of Smart and Nano Materials*, vol. 2, no. 1, pp. 22–38, 2011.

[30] C. Girerd, Q. Zhang, A. Gupta, M. Dunna, D. Bharadia, and T. K. Morimoto, "Towards a wireless force sensor based on wave backscattering for medical applications," *IEEE Sensors Journal*, vol. 21, no. 7, pp. 8903–8915, 2021.

[31] A. Gupta, C. Girerd, M. Dunna, Q. Zhang, R. Subbaraman, T. Morimoto, and D. Bharadia, "WiForce: Wireless sensing and localization of contact forces on a space continuum," in *18th USENIX Symposium on Networked Systems Design and Implementation (NSDI 21)*. USENIX Association, Apr. 2021, pp. 827–844. [Online]. Available: https://www.usenix.org/conference/nsdi21/presentation/gupta

[32] S. K. Gupta, S. Lalwani, Y. Prakash, E. Elsharawy, and L. Schwiebert, "Towards a propagation model for wireless biomedical applications," in *IEEE International Conference on Communications, 2003. ICC'03.*, vol. 3. IEEE, 2003, pp. 1993–1997.

[33] D. Vasisht, G. Zhang, O. Abari, H.-M. Lu, J. Flanz, and D. Katabi, "In-body backscatter communication and localization," in *Proceedings of the 2018 Conference of the ACM Special Interest Group on Data Communication*, 2018, pp. 132–146.

[34] Y. Ma, Z. Luo, C. Steiger, G. Traverso, and F. Adib, "Enabling deep-tissue networking for miniature medical devices," in *Proceedings of the 2018 Conference of the ACM Special Interest Group on Data Communication*, 2018, pp. 417–431.

[35] D. Steck, J. Qu, S. B. Kordmahale, D. Tscharnuter, A. Muliana, and J. Kameoka, "Mechanical responses of ecoflex silicone rubber: Compressible and incompressible behaviors," *Journal of Applied Polymer Science*, vol. 136, no. 5, p. 47025, 2019.

[36] Y.-L. Park, C. Majidi, R. Kramer, P. Bérard, and R. J. Wood, "Hyperelastic pressure sensing with a liquid-embedded elastomer," *Journal of micromechanics and microengineering*, vol. 20, no. 12, p. 125029, 2010.

[37] G. L. McCreery, A. L. Trejos, M. D. Naish, R. V. Patel, and R. A. Malthaner, "Feasibility of locating tumours in lung via kinaesthetic feedback," *The International Journal of Medical Robotics and Computer Assisted Surgery*, vol. 4, no. 1, pp. 58–68, 2008.

[38] E. Series, "Smooth-on, inc." 2013. [Online]. Available: https://www.smooth-on.com/tb/files/ECOFLEX_SERIES_TB.pdf

[39] M. Chemicals, "Safety data sheet," 2017. [Online]. Available: https://assets.testequity.com/te1/Documents/pdf/mg-sds-4902p.pdf

[40] "Smt ultra-miniature coaxial connectors," https://www.farnell.com/datasheets/307202.pdf.

[41] J. M. L. d. Reis, "Effect of temperature on the mechanical properties of polymer mortars," *Materials Research*, vol. 15, no. 4, pp. 645–649, 2012.

[42] G. Zheng, Y. Kang, J. Sheng, Q. Qin, H. Wang, and D. Fu, "Influence of moisture content and time on the mechanical behavior of polymer material," *Science in China Series E: Technological Sciences*, vol. 47, no. 5, pp. 595–607, 2004.

[43] F. Abdollahi-Mamoudan, S. Savard, C. Ibarra-Castanedo, T. Filleter, and X. Maldague, "Influence of different design parameters on a coplanar capacitive sensor performance," *NDT & E International*, vol. 126, p. 102588, 2022.

[44] Z. Liao, M. Hossain, X. Yao, R. Navaratne, and G. Chagnon, "A comprehensive thermo-viscoelastic experimental investigation of ecoflex polymer," *Polymer Testing*, vol. 86, p. 106478, 2020.

[45] J. Couto and W. M. Grill, "Kilohertz frequency deep brain stimulation is ineffective at regularizing the firing of model thalamic neurons," *Frontiers in computational neuroscience*, vol. 10, p. 22, 2016.

[46] C. J. Yang and A. P. Sample, "Em-comm: Touch-based communication via modulated electromagnetic emissions," *Proceedings of the ACM on Interactive, Mobile, Wearable and Ubiquitous Technologies*, vol. 1, no. 3, pp. 1–24, 2017.

[47] R. Ogden and D. Roxburgh, "A pseudo-elastic model for the mullins effect in filled rubber," *Proceedings: Mathematical, Physical and Engineering Sciences*, vol. 455, p. 28612877, 1988.

[48] X. Lv, L. Liu, Y. Liu, and J. Leng, "Electromechanical modeling of softening behavior for dielectric elastomers," *Journal of Applied Mechanics*, vol. 85, no. 11, p. 111010, 2018.

[49] J. Diani, B. Fayolle, and P. Gilormini, "A review on the mullins effect," *European Polymer Journal*, vol. 45, no. 3, pp. 601–612, 2009.

[50] J. Peirs, J. Clijnen, D. Reynaerts, H. Van Brussel, P. Herijgers, B. Corteville, and S. Boone, "A micro optical force sensor for force feedback during minimally invasive robotic surgery," *Sensors and Actuators A: Physical*, vol. 115, no. 2-3, pp. 447–455, 2004.